



FCTUC FACULDADE DE CIÊNCIAS
E TECNOLOGIA
UNIVERSIDADE DE COIMBRA

Development and Implementation of Software for Parametric Quantification in Perfusion Studies of the Liver

Ana Mafalda Sanches Teixeira

MASTER'S DEGREE IN BIOMEDICAL ENGINEERING

Physics Department

Faculty of Sciences and Technology of University of Coimbra

September 2014

Development and Implementation of Software for Parametric Quantification in Perfusion Studies of the Liver

Author

Ana M. S. Teixeira

Supervisor

Dr. Sónia I. Gonçalves

*Dissertation presented to the Faculty of Sciences and Technology of the University
of Coimbra to obtain a Master's degree in Biomedical Engineering*

Coimbra, 2014

This thesis was developed in collaboration with:

ICNAS - Institute of Nuclear Sciences Applied to Health



Esta cópia da tese é fornecida na condição de que quem a consulta reconhece que os direitos de autor são pertença do autor da tese e que nenhuma citação ou informação obtida a partir dela pode ser publicada sem a referência apropriada.

This copy of the thesis has been supplied on condition that anyone who consults it is understood to recognize that its copyright rests with its author and that no quotation from the thesis and no information derived from it may be published without proper acknowledgement.

To my mother and my sister,

Acknowledgments

A realização desta tese de mestrado contou com o apoio e incentivo de várias pessoas, às quais desejo expressar os meus sinceros agradecimentos.

Em primeiro lugar, deixo um agradecimento especial à minha orientadora, Dra. Sónia Gonçalves, por todo o tempo dedicado, pelos conhecimentos transmitidos, pelo profissionalismo demonstrado e pelo apoio incondicional durante todo o projeto.

De seguida gostaria de agradecer à instituição acolhedora do meu projeto, o Instituto de Ciências Nucleares Aplicadas à Saúde (ICNAS) da Universidade de Coimbra, por oferecer as condições necessárias à realização deste projeto. Quero ainda agradecer ao coordenador do curso, o Dr. Miguel Morgado, pelo empenho demonstrado na orientação do curso e por contribuir para que a realização deste tipo de projetos seja possível.

À Adriana, ao Gonçalo e restantes amigos, pelo companheirismo e por todos os momentos diversão. Um especial agradecimento ao Fábio, pela sua presença e pela ajuda constante.

Ao meu avô, à minha irmã, ao Marco e à Dina pelas suas preocupações, conselhos e todo o apoio durante esta fase.

Por fim, o último e mais importante agradecimento vai para a minha mãe por todos os sacrifícios que fez e por ter sempre acreditado nas minhas capacidades. Sem ela não teria chegado até aqui.

Obrigado a todos!

Abstract

Perfusion imaging is a technique that allows the detection of regional and global alterations in an organ blood flow, and can help to predict the onset of many diseases where the organ hemodynamics is modified. The ability of image contrast manipulation through exogenous contrast agents makes MRI a widely used technique for the assessment of liver perfusion in a non-invasive way. However, accurate liver perfusion assessment remains controversial regarding the mathematical model-based approaches than can be used to quantify perfusion. In general, commercially available software packages determine liver perfusion based on the classic and widely used Tofts model. This is a compartmental model that assumes contrast agent exchange between two compartments – blood plasma and tissue – and that there is a single input through which the contrast reaches the organ, and one output. The Tofts model has to suffer adaptations in order to contemplate both arterial and venous blood inputs of the liver. This work aims to develop and implement a software for parametric quantification of perfusion in the liver using a dual-input one-compartment model. Software implementation uses Matlab and it is organized in a series of steps that go from reading raw MRI data to calculating liver perfusion parametric maps. Software tests were conducted in a patient population with hepatocellular carcinoma. Results indicate that the proposed model is able to determine perfusion parameters and is sensitive to the detection of perfusion alterations. Standard image acquisition protocols must be used in the future in order to extend model application to larger clinical populations.

Keywords: magnetic resonance imaging, liver perfusion, Tofts model, dual-input one-compartment model, hepatocellular carcinoma

Resumo

A imagem de perfusão é uma técnica que permite a detecção de alterações regionais e globais do fluxo sanguíneo de um órgão e pode ajudar a prever o aparecimento de muitas doenças, nas quais a hemodinâmica do órgão se encontra modificada. A capacidade de manipulação do contraste da imagem através do uso de agentes de contraste exógenos faz da imagem por ressonância magnética (IMR) uma técnica amplamente utilizada para a avaliação não-invasiva da perfusão sanguínea no fígado. No entanto, a avaliação precisa da perfusão hepática permanece controversa relativamente aos diversos modelos matemáticos que podem ser usados para quantificar a perfusão. A maioria dos programas comercialmente disponíveis determina a perfusão no fígado com base no modelo Tofts, um modelo clássico e muito utilizado. Este é um modelo compartimental que assume troca do agente de contraste entre dois compartimentos - plasma sanguíneo e tecido - e que existe apenas uma entrada através da qual o contraste atinge o órgão, bem como uma saída. O modelo de Tofts tem de sofrer adaptações de modo a contemplar tanto a entrada de sangue arterial bem como a de sangue venoso que se verifica no fígado. Este trabalho pretende desenvolver e implementar um *software* para quantificação paramétrica da perfusão no fígado usando um modelo de duas entradas e um compartimento. O *software* em Matlab contempla o algoritmo desenvolvido num conjunto de passos, começando com a leitura dos dados não processados de ressonância magnética, terminando no cálculo dos mapas paramétricos das constantes cinéticas do agente de contraste e na perfusão total do fígado. Os testes do *software* foram realizados numa população com carcinoma hepatocelular. Os resultados indicam que o modelo proposto é capaz de determinar os parâmetros de perfusão e é sensível à detecção das alterações de perfusão. Protocolos de aquisição padrão devem ser utilizados no futuro a fim de estender a aplicação do modelo para populações clínicas maiores.

Palavras-chave: imagem por ressonância magnética, perfusão do fígado, modelo de Tofts, modelo de duas entradas e um compartimento

Symbols & Abbreviations

Symbols

| | |
|-------------|--|
| B_0 | Static external Magnetic field |
| B_1 | Magnetic field associated with the radiofrequency pulse |
| C_a | Hepatic Artery Contrast Agent Concentration |
| C_e | Extracellular Extravascular Space Contrast Agent Concentration |
| C_L | Liver Contrast Agent Concentration |
| C_p | Portal Vein Contrast Agent Concentration |
| C_P | Blood Plasma Contrast Agent Concentration |
| E | Extraction Fraction |
| K^{trans} | Transfer Constant |
| k_{1a} | Hepatic Artery Inflow Rate Constant |
| k_{1p} | Portal Vein Inflow Rate Constant |
| k_2 | Liver Outflow Rate Constant |
| \vec{M} | Net Magnetization |
| \vec{M}_Z | Net Magnetization Longitudinal component |
| \vec{M}_T | Net Magnetization Transverse component |
| P_a | Arterial Perfusion |
| P_p | Portal Perfusion |
| P_L | Liver Perfusion |
| r_1 | Relaxivity |
| S | Signal Intensity |
| t | Time |
| t' | Dummy Integration time variable |
| $T1$ | Spin-Lattice Relaxation |
| $T10$ | Native Spin-Lattice Relaxation |
| $T2$ | Spin-Spin Relaxation |
| $T2'$ | Relaxation Time due to B_0 inhomogeneities |
| $T2^*$ | Total Transverse Relaxation Time |
| v_e | Extracellular Extravascular Space Volume |
| v_p | Blood Plasma Volume |

| | |
|------------|-----------------------------|
| ω_0 | Larmor Frequency |
| γ | Gyromagnetic Ratio |
| τ_a | Hepatic Artery Transit Time |
| τ_p | Portal Vein Transit Time |
| θ | Flip Angle |

Abbreviations

| | |
|-------|--|
| AFP | Alpha-fetoprotein |
| ASL | Arterial Spin Label |
| BBB | Blood-Brain Barrier |
| CA | Contrast Agent |
| CFS | Cerebrospinal Fluid |
| CT | Computed Tomography |
| CE | Contrast-Enhanced |
| DICOM | Digital Imaging and Communications in Medicine |
| EES | Extravascular Extracellular Space |
| FOV | Field of View |
| FT | Fourier Transform |
| Gpe | Gradient Phase Encoding |
| GRE | Gradient-Echo |
| Gro | Gradient Readout |
| Gss | Gradient Slice Selection |
| HBV | Hepatitis B Virus |
| HCC | Hepatocellular Carcinoma |
| HCV | Hepatitis B Virus |
| MR | Magnetic Resonance |
| MRI | Magnetic Resonance Imaging |
| NASH | Non Alcoholic Steatohepatitis |
| RF | Radiofrequency |
| ROI | Region of Interest |
| PDGFR | Platelet Derived Growth Factor Receptor |
| PET | Positron Emission Tomography |
| PL | Liver Perfusion |
| PM | Parametric Maps |
| SE | Spin-Echo |
| SNS | Signal-to-Noise Ratio |
| TE | Echo Time |
| TR | Repetition Time |

US

Ultrasound

VEGFR

Vascular Endothelial Growth Factor Receptor

List of Figures

| | |
|--|----|
| Figure 1.1: Location of the liver. Adapted from [3] | 3 |
| Figure 1.2: General anatomy of the liver. a) Anterior aspect. b) Posterior aspect. Adapted from [2] | 3 |
| Figure 1.3: Liver circulation network. Bile Ducts, Portal Vein and Hepatic Artery ramifications through the liver parenchyma. Adapted from [6]..... | 5 |
| Figure 1.4: a) Microscopic anatomy of a six-sided lobule with arrows indicating the direction of blood flow (adapted from [7]). b) Representative diagram of the microanatomic relationship of blood cells within sinusoid, fenestrated endothelial cells, plasma (p), the Space of Disse and the hepatocyte (adapted from [6]). | 6 |
| Figure 1.5: Global variation in HCC incidence rates for the year of 2002. Classification was based on data in males being 'Very high incidence' >20 per, 'Moderately high incidence' between 11 and 20, 'Intermediate incidence' between 5 and 10 and 'Low incidence' <5, all per 100,000. Adapted from [10]..... | 7 |
| Figure 2.1: Randomly orientated spins (left) align when exposed to strong external magnetic field, presenting parallel or antiparallel orientations (right). Adapted from [17]. | 12 |
| Figure 2.2: Flip of the net magnetization by 90° after spin excitation with an RF pulse at the Larmor frequency. Adapted from [17]. | 13 |
| Figure 2.3: Relaxation processes. Alignment of the net magnetization with the external magnetic field in longitudinal relaxation (upper row). Dephasing of precessing spins in transverse relaxation (lower row). Adapted from [17]. | 14 |
| Figure 2.4: K-space representation where each pixel corresponds to a specific phase and frequency combination. Adapted from [17]. | 17 |
| Figure 2.5: Spin-echo sequence scheme made up of a series of events: 90° pulse – 180° rephasing pulse at $TE/2$ – signal reading at TE . This series is repeated at each time interval TR . Adapted from [17]. | 18 |
| Figure 2.6: 2-D spoiled gradient-echo scheme. In the absence of the 180° pulse, the polarity of the dephasing gradient pulse is opposite to the readout gradient pulse applied. Adapted from [17]. | 19 |
| Figure 3.1: Schematic representation of the Tofts model. Based on [25]. | 24 |
| Figure 3.2: Schematic representation of the dual-input one-compartment model for liver perfusion. Based on [23] | 25 |
| Figure 3.3: Gadovist chemical structure. It is a macrocyclic neutral Gd-chelate [25]. | 27 |
| Figure 3.4: Flowchart illustrating the major steps of the algorithm that was implemented to estimate perfusion parameters on a pixel-by-pixel basis, using a dual-input one compartmental model. | 29 |
| Figure 3.5: Liver ROIs of the same patient for the slice 13 drawn from the first temporal dynamic, corresponding to pre-treatment (left) and post-treatment (right). Differences in size, location and shape are highlighted..... | 30 |
| Figure 3.6: Abdominal aorta (red), used as substitute for the hepatic artery, and portal vein (blue) ROIs for the same patient. | 30 |
| Figure 3.7: Different signal intensities from T_1 -weighted images with variable flip angles. For T_1 mapping 20° (a), 50° (b), 100° (c), and 150° (d) were used. | 31 |

| | |
|---|----|
| Figure 3.8: Dependence of the signal intensity on the flip angle. The peak of the curve corresponds to the Ernst angle. Based on [28]. | 33 |
| Figure 3.9: a) Anatomical location of the chosen pixel in the artery region. b) Temporal variation of the signal over time (arbitrary units). Identification of a baseline of 3, starting the acquisition at time 4. | 36 |
| Figure 3.10: Example (with non-real values) of the type of structure obtained in the calculation of concentration. Choosing a pixel of coordinates (X,Y), it is possible to access the values of concentration over time (represented by the third dimension). Adapted from [36]. | 40 |
| Figure 4.1: Contrast-enhancement in a liver MR slice from post-treatment acquisition of patient 3: a) pre-contrast; b) “early” contrast-enhancement; c) “late” contrast-enhancement. | 43 |
| Figure 4.2: Typical enhancement signal curves (of arbitrary units) derived from pixels in the tumor and healthy parenchyma regions respectively. | 44 |
| Figure 4.3: Liver (yellow) and tumor (magenta) ROIs of Patient 1 in: a) pre-treatment and b) post-treatment scans. | 45 |
| Figure 4.4: Liver (yellow) and tumor (magenta) ROIs of Patient 2 in: a) pre-treatment and b) post-treatment scans. | 46 |
| Figure 4.5: Liver (yellow) and tumor (magenta) ROIs of Patient 3 in: a) pre-treatment and b) post-treatment scans. | 46 |
| Figure 4.6: Liver (yellow) and tumor (magenta) ROIs of Patient 4 in: a) pre-treatment and b) post-treatment scans. | 46 |
| Figure 4.7: Liver (yellow) and tumor (magenta) ROIs of Patient 5 in: a) pre-treatment and b) post-treatment scans. | 47 |
| Figure 4.8: T_1 parametric maps for Patient 1. | 47 |
| Figure 4.9: T_1 parametric maps for Patient 2. | 48 |
| Figure 4.10: T_1 parametric maps for Patient 3. | 48 |
| Figure 4.11: T_1 parametric maps for Patient 4. | 48 |
| Figure 4.12: T_1 parametric maps for Patient 5. | 48 |
| Figure 4.13: T_1 map of an alternative slice of Patient 4 in post-treatment examination that shows a larger area of the liver with high T_1 values. | 49 |
| Figure 4.14: a) to c) - Identification of the abdominal aorta), portal vein and small segments from tumor and parenchyma ROIs from post-treatment dynamics of Patient 3. d) Average CA concentration-time curves from the displayed ROIs. | 50 |
| Figure 4.15: k_{1a} , k_{1p} , k_2 and PL parametric maps for Patient 1. | 52 |
| Figure 4.16: k_{1a} , k_{1p} , k_2 and PL parametric maps for Patient 2. | 52 |
| Figure 4.17: k_{1a} , k_{1p} , k_2 and PL parametric maps for Patient 3. | 52 |
| Figure 4.18: k_{1a} , k_{1p} , k_2 and PL parametric maps for Patient 4. | 53 |
| Figure 4.19: k_{1a} , k_{1p} , k_2 and PL parametric maps for Patient 5. | 53 |

Contents

| | |
|---|--------------|
| Acknowledgments | xi |
| Abstract | xiii |
| Resumo | xv |
| Symbols & Abbreviations | xvii |
| List of Figures | xxi |
| Contents | xxiii |
| CHAPTER I | I |
| Introduction | I |
| 1.1 <i>Motivation and objectives</i> | <i>I</i> |
| 1.2 <i>Liver: a brief view of anatomy and functions</i> | <i>3</i> |
| 1.2.1 Normal and Abnormal Liver Circulation..... | <i>4</i> |
| 1.2.2 Hepatocellular Carcinoma | <i>6</i> |
| 1.2.2.1 Global Variation and Incidence..... | <i>7</i> |
| 1.2.2.2 Risk Factors and Epidemiology | <i>8</i> |
| 1.2.2.3 Screening, surveillance and diagnosis | <i>9</i> |
| CHAPTER 2 | II |
| Perfusion Studies of the Liver using MRI | II |
| 2.1 <i>Magnetic Resonance Imaging</i> | <i>II</i> |
| 2.1.1 Fundamentals..... | <i>11</i> |
| 2.1.2 Relaxation effects and Bloch Equation | <i>14</i> |
| 2.1.3 Spatial Encoding - Image Formation..... | <i>16</i> |
| 2.1.4 Pulse Sequences..... | <i>17</i> |
| 2.2 <i>Perfusion Imaging</i> | <i>19</i> |
| 2.2.1 CE – MRI for hepatic perfusion study | <i>20</i> |
| 2.2.2 Liver perfusion information from MRI data | <i>21</i> |
| CHAPTER 3 | 23 |
| Materials and Methods | 23 |
| 3.1 <i>Perfusion Models</i> | <i>23</i> |
| 3.1.1 Dual-input one-compartment model..... | <i>25</i> |
| 3.2 <i>Data acquisition</i> | <i>26</i> |
| 3.2.1 Patient Selection and Image Acquisition | <i>26</i> |
| 3.3 <i>Software implementation</i> | <i>28</i> |
| 3.3.1 ROIs definition | <i>29</i> |
| 3.3.2 <i>T1</i> Mapping..... | <i>31</i> |
| 3.3.3 Contrast agent concentration conversion | <i>33</i> |
| 3.3.4 Perfusion Parameters | <i>37</i> |
| 3.3.5 Implementation in Matlab..... | <i>38</i> |

| | |
|--|-----------|
| CHAPTER 4 | 43 |
| Results..... | 43 |
| 4.1 <i>Signal Enhancement and and tumor identification</i> | <i>43</i> |
| 4.2 <i>ROIs definition.....</i> | <i>45</i> |
| 4.3 <i>T1 parametric maps</i> | <i>47</i> |
| 4.3 <i>Contrast Agent Concentration.....</i> | <i>50</i> |
| 4.4 <i>Perfusion Parameters</i> | <i>51</i> |
| CHAPTER 5 | 57 |
| Discussion | 57 |
| CHAPTER 6 | 63 |
| Conclusion | 63 |
| References | 65 |

Chapter I

Introduction

1.1 Motivation and objectives

The liver is an organ with a well-defined vascular structure. There are many hepatic perfusion disorders that induce modifications to the normal liver blood supply. Perfusion imaging of the liver is a quantitative imaging method that reflects the microcirculatory status of hepatic parenchymal and hepatic lesion blood flow. It is used in the clinical evaluation of several hepatic disorders such as cirrhosis or hepatocellular carcinoma (HCC). In the latter case, perfusion studies play an important role in e.g. detection of the primary tumor and metastases, evaluation of tumor viability or assessment of the effectiveness of antiangiogenic therapies.

One of the major advantages of magnetic resonance imaging (MRI) is its wide range of imaging contrasts that provide, noninvasively, valuable information over the anatomy and function of the human body. The use of an exogenous contrast agent (CA) further enhances the flexibility of MRI to detect and study perfusion conditions.

The evaluation of perfusion with MRI is achieved through the analysis of dynamic imaging data with mathematical models that describe the temporal evolution of the contrast agent concentration. By comparing the model predictions with the experimental data, it is possible to calculate the kinetic parameters that describe the transport of the contrast agent from the vascular bed to the extravascular extracellular space and vice-versa. Through the calculation of kinetic parameters one can evaluate perfusion and thereby identify potential biomarkers of disease.

The evaluation of hepatic perfusion with MRI is possible with commercially available software. However, the central question here is that the mathematical models

that are implemented in these software packages generally follow the classic approach as proposed by Tofts and co-workers [1], which assumes the exchange of contrast agent between two compartments with a single input. The latter does not accurately describe the real vascular architecture of the liver and do not take into account the input of blood from the portal vein and consider the blood input to the liver to be mainly arterial.

The present work aims to develop and implement a software for parametric quantification of perfusion using contrast enhanced MRI (CE-MRI) data acquired at 3T and using a gadolinium (Gd) based contrast agent. A dual-input one-compartment model is considered, which takes into account the dual input from both venous and arterial blood vessels, thus better reflecting the real liver blood supply.

The present thesis consists of three main parts. The first part introduces the main concepts of MRI - physics of signal generation, image contrast mechanisms, image acquisition and reconstruction and basic pulse sequences. In this section, a review of the existing models for hepatic perfusion is also presented. The second part of the thesis describes the algorithm that was created to analyze hepatic CE-MRI data with the dual-input single compartment model and the strategy that was followed for software implementation. The third and last part of this work was the validation, in which the developed software was tested in a population with HCC.

1.2 Liver: a brief view of anatomy and functions

The liver is a reddish brown tubular gland located immediately under the diaphragm, filling most of the right hypochondriac and epigastric regions. The under surface faces the stomach, the first part of the duodenum and the right side of the large intestine (figure 1.1) [2, 3]. It is the second largest organ in the human body (second to skin) and the largest internal organ weighting approximately between 1.2 Kg to 1.8 Kg in an adult human [4].

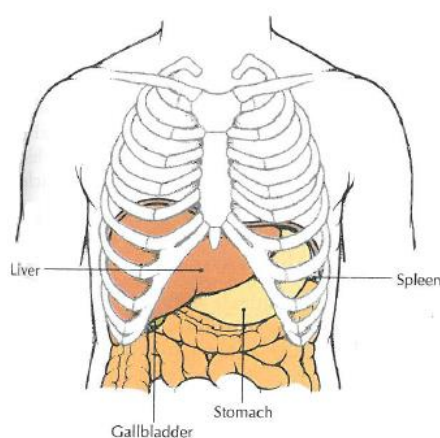


Figure 1.1: Location of the liver. Adapted from [3].

Anatomically the liver has four lobes: the right, left, quadrate and caudate lobes but usually there is a gross division in the two main lobes (left and right) by the falciform ligament (figure 1.2) [3].

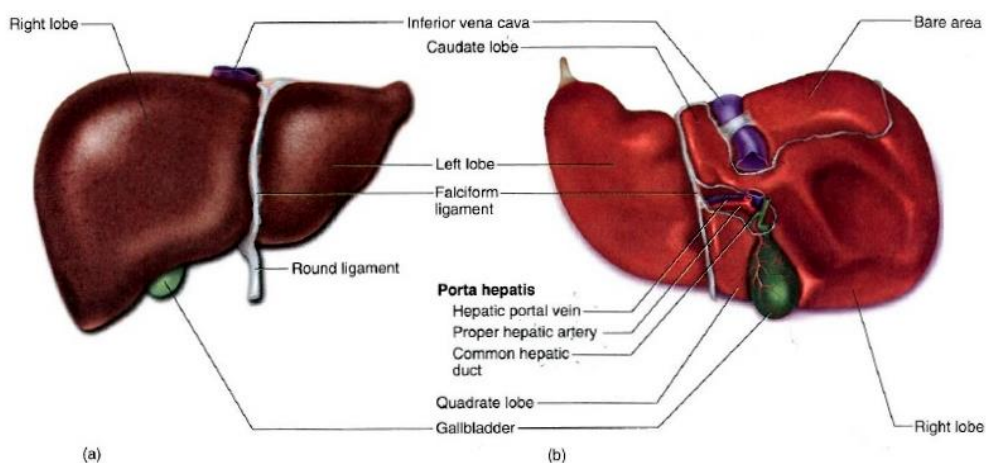


Figure 1.2: General anatomy of the liver. a) Anterior aspect. b) Posterior aspect. Adapted from [2].

At the microscopic level, the functional units are represented by cylindrical structures with about 2 mm long by 1 mm in diameter called hepatic lobules. A lobe consists of a central vein passing down its core, surrounded by radiating sheets of cuboidal cells called hepatocytes. Each corner of the lobule usually contains a portal area, a complex composed of branches of the portal vein, hepatic artery, bile duct and nerve. Between the radiating rows of cells there are dedicated blood channels called sinusoids, which transport blood of the portal vein and hepatic artery. The sinusoids are lined by a fenestrated endothelium with fenestrations so large so that the hepatocytes are in direct contact with the blood. The blood flows from the portal area in the sinusoids and then to the central vein, which drains it from the lobule to the hepatic vein [2, 3].

Though it lies outside the digestive tract, the liver plays a key role not only to digestion but also to the proper functioning of the human organism. Only one of the liver main functions contributes directly to the digestion: the secretion of bile. Other liver main functions are the regulation of the blood glucose levels, lipid synthesis (as lipoproteins, cholesterol and phospholipids), the removal of certain protein metabolism residues (like the NH₂ groups), storage of vitamins (A, D, E, K and B₁₂) and minerals (such as iron and copper) [2, 3].

1.2.1 Normal and Abnormal Liver Circulation

The liver is a highly vascularized organ (figure 1.3) characterized by a dual blood supply consisting of the portal vein, which is the major supplier, contributing with about 75% of the blood input, and the hepatic artery with the remaining 25% of blood input to the liver [5]. The hepatic artery supplies the liver with oxygenated arterial blood, while the hepatic portal vein drains venous blood from the entire gastrointestinal tract containing the nutrients absorbed by the small intestine. The output blood function is performed by the hepatic vein that drains blood from the liver into the inferior vena cava. There are also bile ducts which collect bile from the liver cells [2].

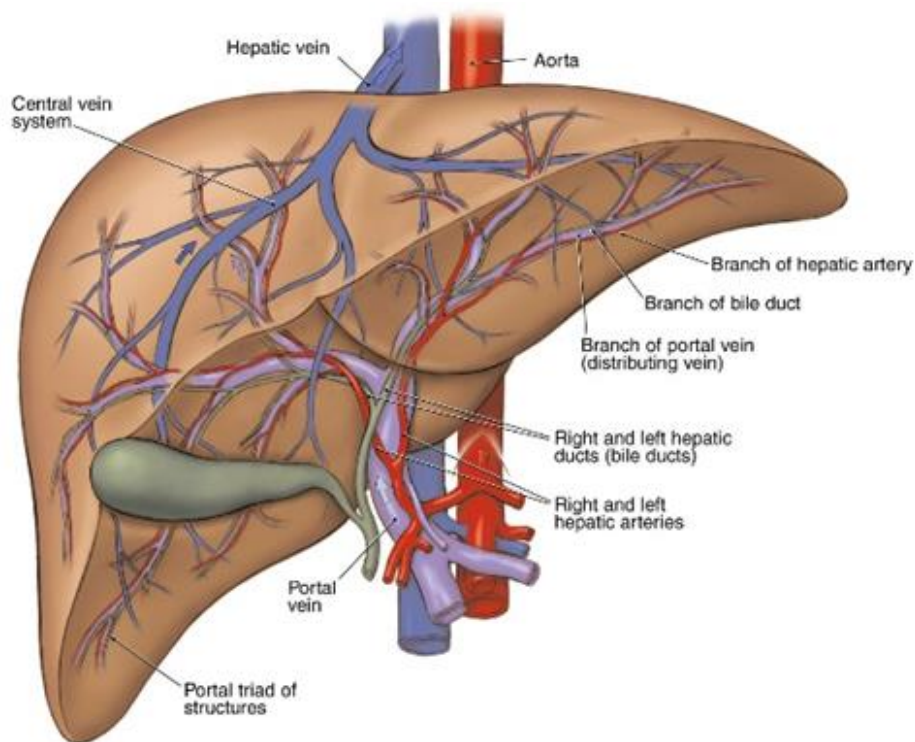


Figure 1.3: Liver circulation network. Bile Ducts, Portal Vein and Hepatic Artery ramifications through the liver parenchyma. Adapted from [6].

The arterial and venous supplies to the liver are not independent systems. Both of them provide blood, at different times, to the low pressure-sinusoids. These are lined with highly fenestrated endothelial cells, flanked by the hepatocytes in the liver cords (figure 1.4a). A nutrient-laden venous blood from the intestines and freshly oxygenated arterial blood from the celiac trunk is therefore delivered to the hepatocytes [3].

This anatomical arrangement allows therefore the plasma to flow freely through the sinusoidal endothelial cells into the small interstitial space between sinusoidal endothelium and hepatocytes, known as the Space of Disse. Under normal conditions, the large size of the sinusoids' fenestrae allows free exchange of low-molecular-weighted compounds between the plasma sinusoids and the interstitial Space of Disse (figure 1.4b). After filtering through the sinusoids, this blood collects in the central vein and drains to the hepatic veins which lead to the inferior vena cava [7].

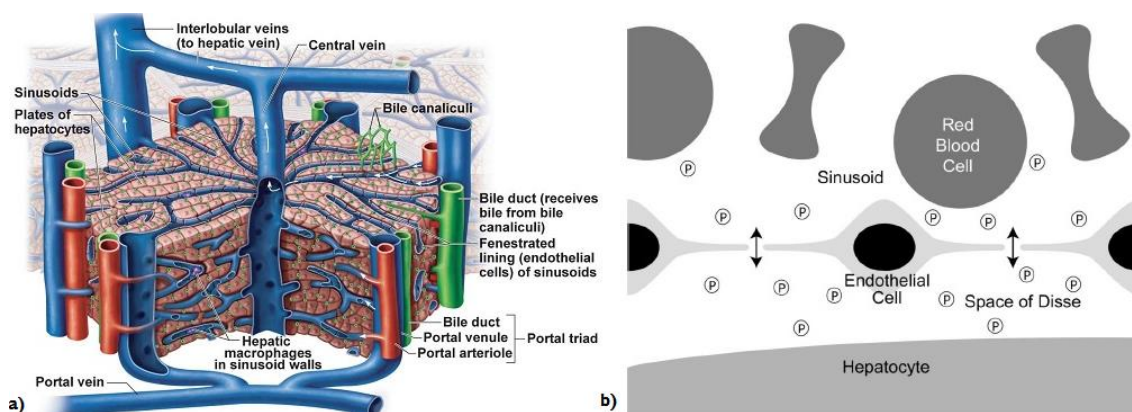


Figure 1.4: a) Microscopic anatomy of a six-sided lobule with arrows indicating the direction of blood flow (adapted from [7]). b) Representative diagram of the microanatomic relationship of blood cells within sinusoid, fenestrated endothelial cells, plasma (p), the Space of Disse and the hepatocyte (adapted from [6]).

In abnormal situations, more particularly in liver tumours such as hepatocellular carcinoma and metastases, there are relative changes in arterial and portal blood supply.

Initially the blood supply from the liver to the tumor is due to the proliferation of the sinusoidal cells that become capillarized with loss of fenestrae and with the formation of basement membrane. As the tumor continues to grow and developing metastases, there is a combined process of recruitment of new blood vessels to the tumor region, supplied by the hepatic artery, which is called neoarteriogenesis. These modifications lead to a significant barrier to the free passage of low-molecular-weighted compounds between the plasma and the tumor region [5]. This feature is helpful in the way that such changes may be reflected in the hepatic enhancement kinetics of low-molecular-weighted contrast agents used in some imaging techniques like the dynamic contrast-enhanced magnetic resonance imaging (CE MRI) [8].

1.2.2 Hepatocellular Carcinoma

The Hepatocellular Carcinoma (HCC) is one of the most common, corresponding to approximately 70 – 80% of all liver tumors. The poor prognosis and late detection causes this to be the third-leading cause of cancer-related death worldwide. This is an aggressive cancer with a poor survival rate, being the incidence

almost equal to the death rate, responsible for approximately 600,000 deaths annually all over the world [6, 9, 10].

1.2.2.1 Global Variation and Incidence

HCC incidence keeps increasing with a unique geographic, sex and age distribution. Data analysis from large patient populations is a useful tool to study possible causes and trends. Looking to age-standardized incidence cases of HCC grouped by region and gender (figure 1.5), it is possible to notice that areas corresponding to 'very high' and 'moderately high' incidence include China, southeastern Asia, sub-Saharan western and eastern Africa. In most developed parts of the world, including Europe and North America, the incidence is very low with exception of Southern Europe and Japan. It is also noted a curious characteristic of the disease: higher incidence in men than in women [9, 10].

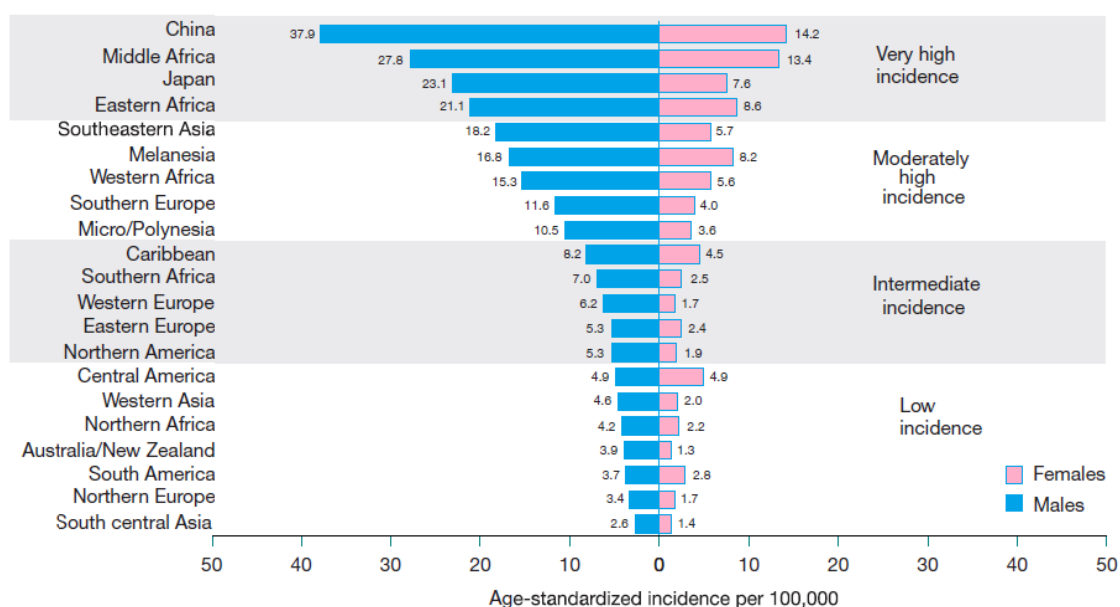


Figure 1.5: Global variation in HCC incidence rates for the year of 2002. Classification was based on data in males being 'Very high incidence' >20 per, 'Moderately high incidence' between 11 and 20, 'Intermediate incidence' between 5 and 10 and 'Low incidence' <5, all per 100,000. Adapted from [10].

1.2.2.2 Risk Factors and Epidemiology

The HCC is a complex malignancy with associated risk factors. In most cases there is a close relation with previous episodes of chronic infections such as viral or alcoholic liver disease [10, 11]. Within the main risk factors are:

- ❖ Hepatitis Viruses: The vast majority of primary liver tumor (75 – 80 % of the cases) originate from viral infections: either from hepatitis B virus (HBV) or from hepatitis C virus, being the HBV more frequent [11].
- ❖ Alcohol: Chronic alcohol abuse and alcoholic cirrhosis are known risk factors to HCC. The threshold dose and the exposure time that may lead to the disease are unknown. One of the hypothesis alcohol related HCC is that alcohol acts as a carcinogenic cofactor in the presence of HBV or HCV infection [9, 11].
- ❖ Nonalcoholic Steatohepatitis (NASH): The exact incidence of HCC in patients with NASH is also unknown. However there is a close positive correlation of the incidence of HCC with obesity and diabetes. These two conditions are usually related to the development of NASH, an increasingly recognised cause of cirrhosis, the latter representing one of the main risk factors for the development of HCC [11, 12].
- ❖ Chemical carcinogens: There is a close relationship between the exposure to aflatoxin B₁ and the development of HCC. Aflatoxin is natural chemical carcinogen, produced by the *Aspergillus* fungus, which can be found in stored grains (such as peanuts and rice) in hot humid places. Aflatoxin contamination of food relates well with the incidence rates in Africa and China. There are other carcinogens that can also be responsible for the increased incidence of HCC like pesticides and insecticides seen in the middle East [6, 9].
- ❖ Other conditions: Metabolic disorders (like hemochromatosis and Wilson's disease), chronic autoimmune liver diseases and several other underlying conditions have a less common association to de appearance of HHC. However,

they should be taken into consideration since they can be considered risk conditions. In any case, etiology of HCC in most patients who do not have cirrhosis or viral infections is still unclear [6, 11].

1.2.2.3 Screening, surveillance and diagnosis

Liver cancers may often escape clinical recognition due to the fact that they often arise in patients with cirrhosis. Symptoms attributed to the emergence of the disease are usually absent and, when present, are not specific of HCC. Among other complaints are: abdominal and epigastric pain, weight loss, early food satiety, nausea and abdominal swelling. As the evolution of the disease is usually fast and fatal, most patients are diagnosed at a stage when the disease is already advanced. As a consequence, the hypothesis of using curative therapies is precluded [11, 13].

Periodical surveillance is therefore recommended for those patients considered to be at high risk of developing HCC. The assumption is that early detection may lead to timely therapeutic intervention and to the decrease of associated mortality.

The most common screening methods of HCC are the serologic evaluation of alpha-fetoprotein (AFP) and abdominal ultrasonography (US). Despite of the low sensitivity ($\approx 60\%$), US has great specificity ($>90\%$) in the detection of HCC nodules. Continuously high levels AFP (>500 ng/mL) are known to be associated with the presence of the disease. Due to the low sensitivity of this serologic screening test, it is often associated with US, to increase the reliability of the diagnosis [11].

The modalities of diagnosis depend both on the lesion size and on the underlying liver function. The detection of liver lesions that are larger than 1 cm, using the above mentioned techniques justify the requirement for cross-sectional imaging techniques. Blood supply of HCC lesions is different from the surrounding healthy hepatic parenchyma, being that the tumor is supplied by the hepatic artery whereas healthy parenchyma is essentially supplied by the portal vein. Based on this, the use of helical computed tomography (CT) and CE-MRI have been establishing a classic image profile of HCC lesions, through the differences between the enhancement profiles of lesions

and healthy parenchyma [11]. In fact, tumor regions not only have early enhancement relatively to the remaining hepatic parenchyma, but they also have a faster washout of the contrast agent.

Chapter 2

Perfusion Studies of the Liver using MRI

2.1 Magnetic Resonance Imaging

2.1.1 Fundamentals

MRI is a versatile imaging technique whose name derives from the Nuclear Magnetic Resonance physical phenomenon in which, through the combination of strong magnetic fields and radiofrequency signals, it is possible to manipulate the precession movements of atoms with intrinsic magnetic susceptibility [14]. With this imaging modality it is possible to create images of biologic tissues that can be used for biomedical purposes.

Atoms that have an odd number of protons or neutrons like hydrogen, carbon-13, fluorine, sodium and phosphorus, behave like a magnetic dipole having associated a magnetic dipole moment, or simply magnetic moment. This non-null magnetic moment interacts with external magnetic fields, allowing its use in MRI. Due the fact that approximately 70% of the human organism is made of water, the preferred imaging element is the hydrogen, composed by a single proton and electron. It can be found not only in free water, but also in macromolecules such as proteins and lipids [14].

Spin is a quantic property, characteristic of sub-atomic particles like protons. It can be seen as the gyratory movement of the proton around its axis. This movement creates a current loop which, in addition to creating a magnetic field itself, is capable of interacting with external magnetic fields [14, 15]. In the absence of an external magnetic field, the proton spins behave like small magnetic dipoles, with a magnetic moment $\vec{\mu}$ of equal magnitude and are randomly oriented in space. When exposed to a static magnetic

field B_0 , they lign-up with the field direction with either parallel or anti-parallel orientations. However, there is a small excess of spins aligned parallel to the magnetic field, when compared to those aligned anti-parallel to B_0 . Furthermore, the relative excess of spins depends on factors such as B_0 magnitude and absolute temperature. As a consequence, at normal body temperature and for the typical values of B_0 available in clinical scanners, the net magnetization in equilibrium \vec{M}_0 will be aligned parallel to B_0 [14–16].

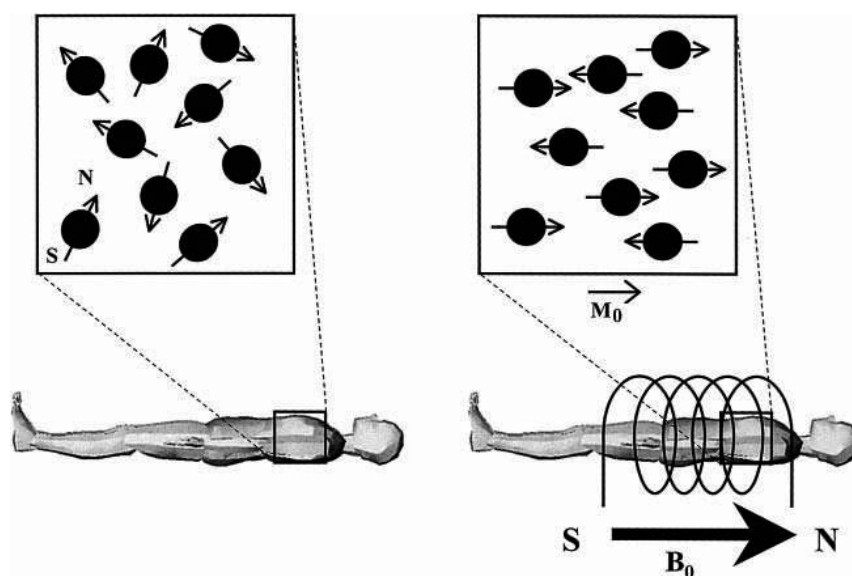


Figure 2.1: Randomly orientated spins (left) align when exposed to strong external magnetic field, presenting parallel or antiparallel orientations (right). Adapted from [17].

Spins describe a precession movement around the axis defined by B_0 . The precession frequency ω_0 , also known as Larmor frequency [15], depends on the gyromagnetic ratio γ and on the strength of the external magnetic B_0 , according to:

$$\omega_0 = \gamma B_0$$

2.1

As the net magnetization \vec{M} contains potential energy, the intentional perturbation of the equilibrium state generates of a measurable signal. Hence, by applying

energy through a radiofrequency magnetic field (B_1) for a short time, i.e., a radiofrequency (RF) pulse with frequency equal to the Larmor frequency ($\omega_{RF} = \omega_0$), a resonance condition is established. In this condition, spins absorb energy from the RF pulse which causes spins to increase their precession angle. This implies that the net magnetization is tipped away from the longitudinal axis, thus creating measurable magnetization, spinning on an axis perpendicular to B_0 and to B_1 . In this way, two magnetization components are obtained: the longitudinal \vec{M}_Z and the transverse \vec{M}_T , parallel and perpendicular to B_0 , respectively [14, 15, 17].

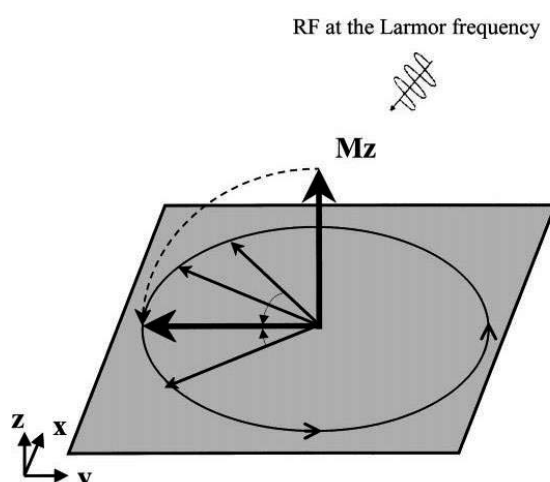


Figure 2.2: Flip of the net magnetization by 90° after spin excitation with an RF pulse at the Larmor frequency. Adapted from [17].

Once the RF is removed, spins tend to come back to its previous equilibrium state through a process called relaxation, which results from the loss of the transmitted RF energy due to the interaction of the nucleus with the system. While \vec{M}_Z recovers to its initial equilibrium state (longitudinal relaxation), \vec{M}_T returns to zero, at a different rate [14, 16]. The magnetization variation, which results from both transverse and longitudinal relaxations, generates the RF signal that is received by coils within the MR scanner. This signal will give information related to the nucleus environment and, if properly encoded, will also give structural information [16].

2.1.2 Relaxation effects and Bloch Equation

After excitation, spins release the absorbed energy, thus returning to the initial state through relaxation. The latter consists of longitudinal and transverse relaxation processes [18].

Longitudinal relaxation, or spin-lattice relaxation is directly related to the realignment of the longitudinal magnetization with the external magnetic field by the liberation of energy to the surroundings. The constant $T1$ is defined as the time that is necessary for the system to recover approximately 63% of the original \vec{M}_z . The values of $T1$ constant, which vary with B_0 intensity and with the type of biologic tissue, can go from hundred to thousands of milliseconds. The cerebrospinal fluid (CSF), blood and grey matter present the highest $T1$ values that can be found in the human body, being the lower ones correspondent to fat [15–18].

Transverse relaxation, or spin-spin relaxation originates from the loss of phase coherence of precessing spins in the transverse plan. Spins have different Larmor frequencies induced by local field inhomogeneities which decrease transverse magnetization and lead to a reduction of signal intensity. This relaxation process is characterized by the $T2$ time constant, defined as the time that elapses until the signal originated from transverse magnetization has reached 37% of its initial value. The values of $T2$ time constants also depend on the magnetic field strength and on the biological tissue and are always smaller than $T1$ values [15–18].

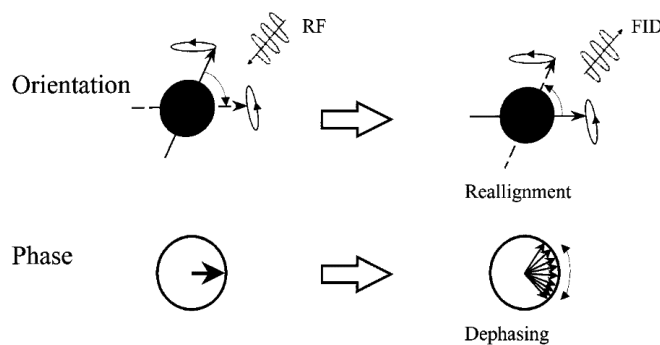


Figure 2.3: Relaxation processes. Alignment of the net magnetization with the external magnetic field in longitudinal relaxation (upper row). Dephasing of precessing spins in transverse relaxation (lower row). Adapted from [17].

The presence of local variations in the external B_0 magnetic field induces a distinct mechanism of transverse relaxation, which is described by the time constant $T2'$. As a consequence, the transverse relaxation time in this situation i.e. $T2^*$, results from the sum of the spin system contribution and that of B_0 and is given by [15]:

$$\frac{1}{T2^*} = \frac{1}{T2} + \frac{1}{T2'} \quad 2.2$$

In the presence of both longitudinal and transverse relaxations, the variation of M_z and M_T is respectively given by [15]:

$$\frac{dM_z}{dt} = \frac{1}{T1} (M_0 - M_z) \quad 2.3$$

And

$$\frac{d\vec{M}_T}{dt} = \gamma \vec{M}_T \times \vec{B}_0 - \frac{1}{T2} \vec{M}_T \quad 2.4$$

The combination of differential equations 2.3 and 2.4, yields the temporal variation of net magnetization vector \vec{M} :

$$\frac{d\vec{M}}{dt} = \gamma \vec{M}_T \times \vec{B}_0 + \frac{1}{T1} (M_0 - M_z) \hat{z} - \frac{1}{T2} \vec{M}_T \quad 2.5$$

The differential equation in 2.5 is known as the Bloch equation and it describes the behaviour of the net magnetization vector in the presence of relaxation effects and for an external magnetic field B_0 pointing along the \hat{z} -axis [15].

2.1.3 Spatial Encoding - Image Formation

Spatial Encoding is the process by which the information from the detected signal, which varies in time, is transformed into signal variation in space. Through the application of field gradients, the resonance frequency changes according to:

$$\omega(x) = \gamma B(x)$$

2.6

Where x corresponds to the spatial coordinate along the gradient field direction and $B(x)$ is the magnetic field in x position [15].

Based on equation 2.6, spectral frequencies will represent the spatial information since they will vary in space according to the prescribed magnetic field gradients. Using a signal processing tool like the inverse Fourier Transform (FT) it is possible to reconstruct the signal and create images from the spectrum of detected frequencies [16, 17]. Spatial Encoding is processed using field gradients in three orthogonal directions: Slice selection gradient (G_{ss}); Phase encoding (G_{pe}) and Frequency encoding/Readout (G_{ro}) gradient [16, 17].

For a given slice to be imaged, a magnetic gradient is added along the slice direction. Due to this spatial variation of the magnetic field, each nucleus will have a Larmor frequency dependent of its position, making possible the selective excitation of a thin slice to be imaged [15–17]. To obtain information for the individual points (pixels) within a slice, the G_{ro} and G_{pe} are used enabling the encoding of both spin frequency and phase, respectively. During phase encoding, a temporary gradient is applied between the RF excitation pulse and the readout, causing a shift in the phase of the precessing nuclei. Changing the amplitude of the temporary gradients, it is possible to acquire signals with different phase encodings [15–17]. The G_{ro} (frequency encoding in x-direction) is used to distinguish pixels within the same phase encoding. This gradient is applied during the readout of the signal and results in a specific shift of the resonance frequency for pixels with the same phase shift [15–17]. The phase and frequency information are stored in the k-space (figure 2.4), where each row corresponds to the frequency

information and each column corresponds to the phase information. Image reconstruction is performed by calculating the 2D (or 3D, if pure three dimensional acquisition) inverse Fourier Transform (FT) of the samples gathered in k-space [14].

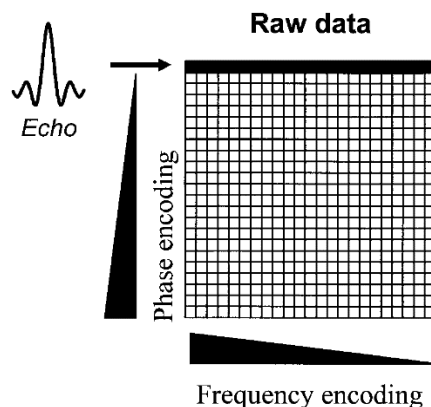


Figure 2.4: K-space representation where each pixel corresponds to a specific phase and frequency combination. Adapted from [17].

2.1.4 Pulse Sequences

MRI uses pulse sequences (RF pulses interleaved with gradients pulses) to obtain images. Through the manipulation of the type, timing and duration of the pulse sequence elements, it is possible to generate different image contrasts (e.g. choosing between T_1 or T_2 weighting) thus potentially increasing the specificity of the study. It is therefore important to tune three parameters involved in the manipulation of pulses sequences: the time between two consecutive RF pulses, known as repetition time (TR), the time between the excitation pulse and the measurement of maximum signal, called echo time (TE) and the flip angle (θ) defined as the angle by which the magnetization is tipped away from B_0 by the application of the RF pulse [15].

There are two main families of pulse sequences: Spin-Echo (SE) and Gradient-Echo (GRE) [15].

Spin-echo sequences (figure 2.5) are characterized by the application of an RF pulse that flips the magnetization 90° from its equilibrium direction followed by a 180° refocusing pulse applied at $TE/2$ and the process is repeated after a certain TR [18, 19].

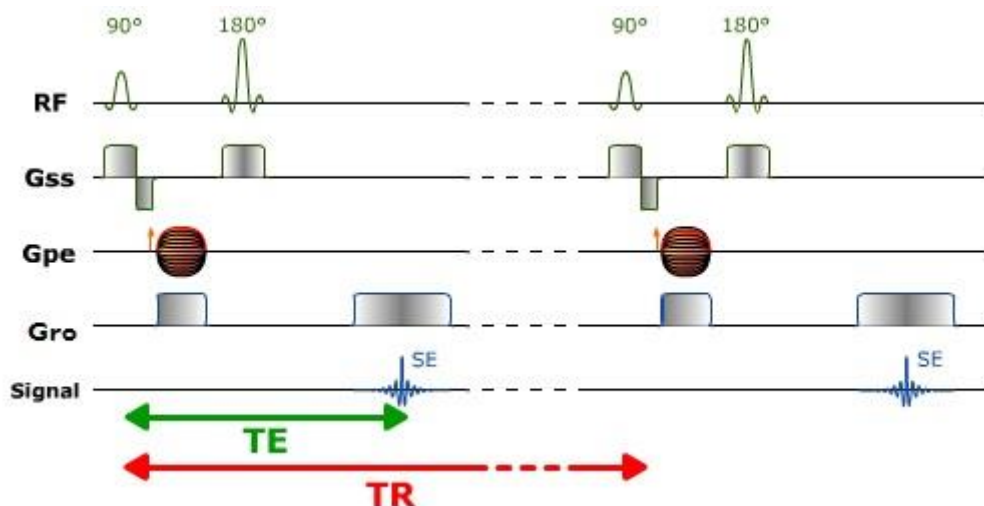


Figure 2.5: Spin-echo sequence scheme made up of a series of events: 90° pulse – 180° rephasing pulse at $TE/2$ – signal reading at TE . This series is repeated at each time interval TR . Adapted from [17].

Gradient-echo sequences (figure 2.6) differ from the spin-echo sequences because they do not use the 180° refocusing pulse and flip angles are usually lower than 90° . Instead of the 180° RF pulse they use a reversal of magnetic field gradients for magnetization refocusing and signal generation. A bipolar readout gradient (frequency-encoding gradient) is required to create an echo. The gradient echo formation results from applying a dephasing gradient before the frequency-encoding or readout gradient. Generally these type of sequences with low-flip angle excitations are faster than the spin-echo sequences, allow new contrasts between tissues (e.g. $T1/T2$) and the resulting images can be weighted on $T1$ or $T2$ [18, 19].

In this work, the type of pulse sequence that is used to acquire data belongs to the gradient-echo type. The effects of $T2^*$ have to be minimized in order to obtain $T1$ -weighting. The choice of a very short TE reduces any $T2$ contrast such that:

$$TE \ll T2 \Rightarrow e^{-\frac{TE}{T2}} \rightarrow 1$$

2.7

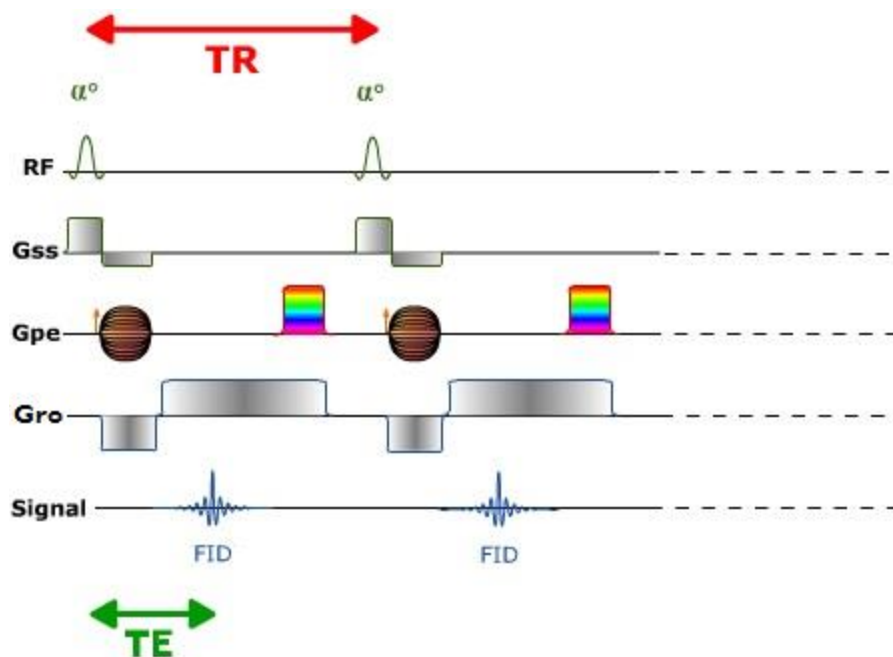


Figure 2.6: 2-D spoiled gradient-echo scheme. In the absence of the 180° pulse, the polarity of Gro dephasing gradient pulse is opposite to the readout gradient pulse applied. Adapted from [17].

2.2 Perfusion Imaging

Perfusion imaging can be defined as a quantitative imaging method that is used to evaluate regional and global modifications in the blood flow of an organ. Since modifications in both arterial and venous blood supplies can predict the onset of disease, hepatic perfusion studies are endowed with great utility as they allow the increase of sensitivity and specificity in disease diagnosis [7, 8].

There are several critical points to perform perfusion studies [7]:

- ❖ High spatial and temporal resolution to identify perfusion differences in small tumors and record the passage of contrast agent, respectively. These two demands are often conflicting.
- ❖ Good image tracer in order to obtain accurate perfusion quantification.
- ❖ Proper tracer kinetic modelling methods for accurate calculation of perfusion parameters.

- ❖ Whole liver imaging enabling tumor surveillance.

2.2.1 CE – MRI for hepatic perfusion study

Despite the existence of various techniques to study blood perfusion, MRI emerges as an interesting one. In fact, this is a high spatial and temporal resolution technique that provides anatomical information, does not make use of ionizing radiation, has good sensitivity for tumor detection and can be combined with other imaging techniques, like positron emission tomography (PET), in order to obtain complementary information [8].

Among several MRI methods to study blood perfusion (arterial spin labelling – ASL [8], for example), the technique which has been established as the gold standard for hepatic perfusion is CE – MRI. It involves the injection of a contrast agent with subsequent MR signal acquisition over time. The signal temporal variation shows the uptake rate of contrast in tissues and its subsequent washout [8].

Contrast agents used in MRI have different magnetic properties that affect hydrogen atoms in water molecules, causing changes to the measured signal. They are used in order to improve both specificity and image signal-to-noise ratio (SNR). The vast majority uses chelates containing paramagnetic atoms having one or more unpaired electrons, creating a strong electronic magnetic moment [20]. Gadolinium, a chemical element of symbol Gd and atomic number 64, is one of the paramagnetic agents that is most used in MRI contrast agents. It has large paramagnetic susceptibility and rapidly redistributes into the extracellular space, thus making it a good contrast agent for perfusion studies. The local magnetic field created by the Gd chelates can relax the magnetic state of the hydrogen atoms, causing modifications in their T_1 relaxation times. Causing T_1 shortening there will be enhanced signal on post-contrast T_1 -weighted images in those regions with highest contrast agent uptake. The pharmacokinetic behavior of the contrast agent is usually defined by the compound chelated to the paramagnetic atom [20].

Liver imaging in CE-MRI uses a dynamic fast MRI sequence, capable of picking up local alterations, which results from the passage of the contrast agent through the liver. Since gadolinium is paramagnetic and leads to the shortening of T_1 , T_1 -weighted sequences are used. Usually, a fast T_1 -weighted spoiled gradient echo sequence is used to acquire the dynamic data series after contrast injection, with coronal or sagittal views [20]. Subsequently, acquired images will show enhancement in areas where contrast was delivered to the tumor [8, 20].

2.2.2 Liver perfusion information from MRI data

Once acquired, MRI data must be analysed in order to extract meaningful vascularity information. The method of analysis depends on factors such as the pulse sequence that is used to acquire data, and the goal of the hepatic perfusion studies. Dynamic MRI data can either be processed using model-free or model-based approaches. Whereas a model-free approach is easier to implement, the results it yields are site dependent as they depend on the MR scanner, the model-based method is more attractive because it gives quantitative information of tissue vascular properties, by using mathematical models that reflect the underlying pathophysiology [8]. Furthermore, the quantification is independent of the MR scanner that was used in data acquisition.

Chapter 3

Materials and Methods

3.1 Perfusion Models

The calculation of perfusion parameters is accomplished through the model-based analysis of MRI data. The use of mathematical models to study vascular leakage and permeability is not a new technique. It had been first used to study perfusion of the functional state of the blood-brain barrier (BBB) in multiple sclerosis disease and brain tumors, as well in retinal disease and breast tumors [1, 21]. With the increase of perfusion studies, several different models have been developed, based on the quantitative analysis of a dynamic curve of signal enhancement versus time from a specific ROI. The versatility of parameter extraction is based on the fact that different model assumptions, reflecting the underlying physiological conditions, can be made.

The most commonly used and well accepted model reflecting the kinetics of low molecular Gd-chelates is the Tofts Model [21]. This is a compartmental model based on the following assumptions [1, 21, 22]:

- Compartments contain the contrast agent in a uniform concentration in all their extension;
- There is an intercompartment flux, which is proportional to the difference of contrast concentration between the compartments;
- *Blood-Plasma* compartment, characterized by a contrast concentration C_p (mM liter⁻¹);

- An *Extravascular Extracellular Space* (EES) compartment, with volume v_e per unit of tissue and tracer concentration C_e .

This is a two-compartment one-input compartmental model, as figure 3.1 shows. Tofts model assumes contrast exchange between two compartments: the Blood plasma and the Tissue with only one vascular input (derived only from hepatic artery, in the liver situation) and one output. There is a main kinetic constant, the transfer constant - K^{trans} (min^{-1}) - that reflects the volume transfer between the plasma (of volume v_p) and the EES (of volume v_e).

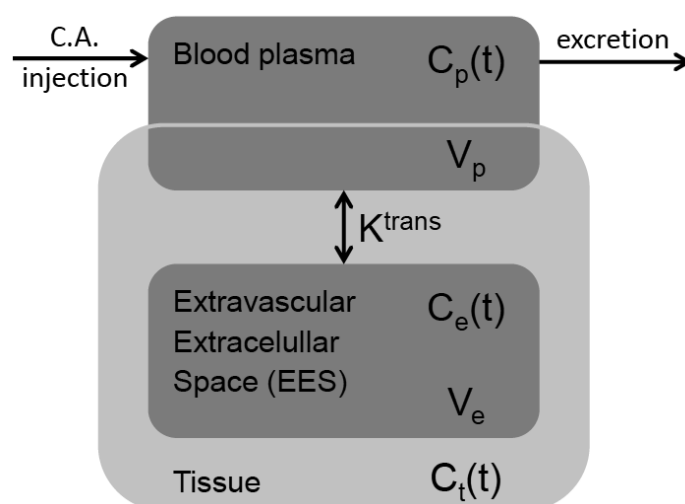


Figure 3.1: Schematic representation of the Tofts model. Based on [25].

Although the Tofts model is well established and used by most commercial software packages for perfusion assessment, the fact is that it does not reflect the real vascular architecture of the liver. This work aims to implement a software for the calculation of liver perfusion parametric maps using a mathematical model that more closely reflects the real vascular architecture of the liver. The proposed model consists of a dual-input one-compartment model, comprising both arterial and portal blood input to the liver.

3.1.1 Dual-input one-compartment model

The Tofts model relies on the fact that the blood input is mainly arterial. This assumption, proved to be wrong in the liver situation, which leads to the necessity of a new formulation in order to produce an accurate calculation of liver perfusion parameters.

A dual-input one-compartment model [23] is presented (figure 3.2). This model reflects the dual input blood flow with two different first-order inflow rate constants: k_{1a} from the hepatic artery and k_{1p} from the portal vein, and a single first-order outflow rate constant k_2 . It is assumed that there is only one compartment corresponding to the liver. Vessels, capillaries, extravascular space hepatic cells are considered to be a single compartment. This assumption can be made because most diffusible contrast agents pass from the capillaries into the extracellular extravascular space, where it remains, until elimination occurs, not being absorbed by hepatocytes. It should be noticed however that for certain types of contrast agents, such as Gd-based contrast agents, this assumption does not hold because the contrast agent is taken in by the hepatocytes. If the purpose of the study was the assessment the functionality of liver cells instead of blood perfusion, a model with more than one compartment would be appropriate.

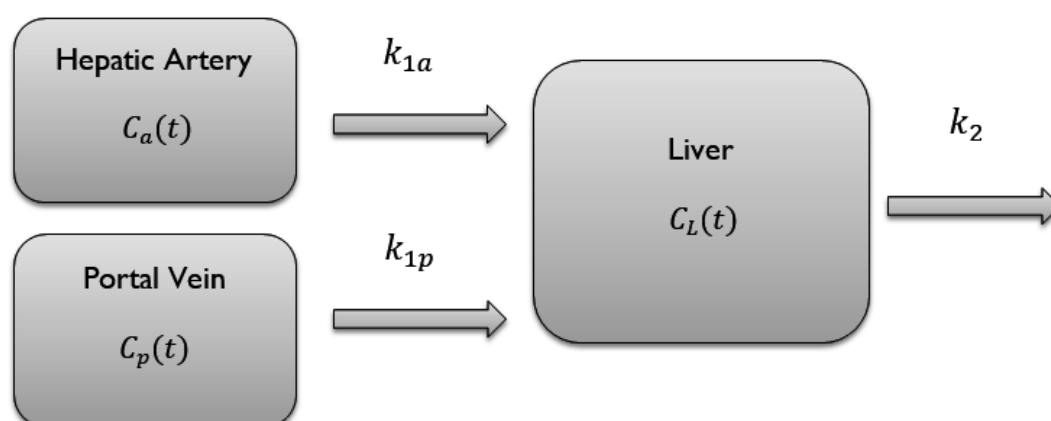


Figure 3.2: Schematic representation of the dual-input one-compartment model for liver perfusion. Based on [23]

$C_a(t)$, $C_p(t)$ and $C_L(t)$ represent the concentration of the tracer from the aorta, the portal vein and the liver compartments, respectively. From this model, the temporal variation of the contrast agent concentration in the liver is given by [23]:

$$\frac{dC_L(t)}{dt} = k_{1a}C_a(t) + k_{1p}C_p(t) - k_2C_L(t) \quad 3.1$$

In this model, perfusion is quantified according to the following equations:

$$\bullet \quad P_a = \frac{k_{1a}}{E} \quad 3.2$$

$$\bullet \quad P_p = \frac{k_{1p}}{E} \quad 3.3$$

$$\bullet \quad P_L = \frac{k_{1a} + k_{1p}}{E} \quad 3.4$$

Where P_a , P_p and P_L are the arterial, portal and liver perfusion usually presented in the literature with units of min^{-1} and E has no units and represents the extraction fraction of the contrast agent in the liver.

3.2 Data acquisition

3.2.1 Patient Selection and Image Acquisition

CE - MRI data from 5 patients (4 male and 1 female), diagnosed with HCC, were used. Participants were included between September 2013 and May 2014 with data acquisition performed twice: before treatment and after approximately 3 months of a treatment with Sorafenib. Sorafenib is an approved drug for the treatment of HCC as well as renal cell and radioactive iodine resistant advanced thyroid carcinomas. It is a multikinase inhibitor that blocks the receptor tyrosine kinases VEGFR (Vascular Endothelial Growth Factor Receptor) and PDGFR (Platelet Derived Growth Factor

Receptor) co-marketed by *Bayer* and *Onyx Pharmaceuticals* as *Nexavar*. *Sorafenib* treatment induces autophagy, which is a process that may lead to tumor growth suppression [24].

Gadovist, *Gd-DO3A-brutol* (figure 3.3), was the nonionic paramagnetic agent used for tissue contrast enhancement during the signal acquisition. It is eliminated by the kidneys [25].

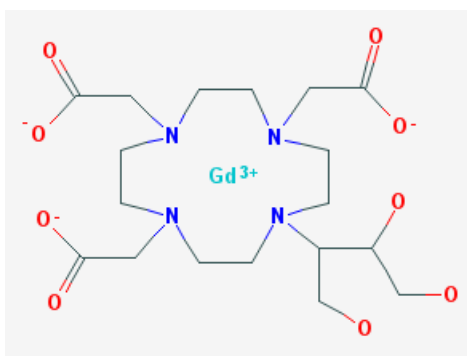


Figure 3.3: Gadovist chemical structure. It is a macrocyclic neutral Gd-chelate [25].

Images were acquired on a 3T whole-body MRI scanner (Siemens MagnetomTrio, Erlangen, Germany).

CE images were acquired for each patient with a 3D T_1 -weighted spoiled gradient-echo in the coronal plane. Additional pulse sequence parameters are shown in *table 1*. Data from each patient consists of a set of 50 dynamics with a specific duration, defined by the temporal resolution, in which the first four/five correspond to the baseline signal from tissues without contrast and the remaining to the temporal variation of the signal after injection of contrast agent. In each dynamic, images of 20 slices are acquired, corresponding to coronal views of the abdominal region. These slices include different sections of the liver tumor, parenchyma and vessels. There was also the acquisition of pre-contrast scans with the same geometry and acquisition plane of the dynamic scans, and where the flip angle was varied from scan to scan. Data acquired in the pre-contrast scans was used to determine the native T_1 of tissues.

Images were exported from the MR scanner in dicom format with a spatial resolution of 128×128 pixels.

Table 1: Pulse sequences parameters for the 3D $T1$ -weighted spoiled gradient-echo scans in both pre- and post-treatment for all patients.

| Patient Nr | Acq. | Baseline Dynamics | Temporal Resolution (ms) | FOV (mm) | Acq. Matrix | In-plane spatial resolution (mm) | Slice Thickness (mm) | Flip Angle (°) | TR (ms) | TE (ms) |
|------------|------|-------------------|--------------------------|----------|-------------|----------------------------------|----------------------|----------------|---------|---------|
| 1 | Pre | 5 | 7857 | 320*320 | 128*128 | 2,50 | 3,60 | 25,0 | 5,80 | 1,12 |
| | Post | 10 | 7855 | 320*320 | 128*128 | 2,50 | 3,60 | 25,0 | 5,80 | 1,12 |
| 2 | Pre | 3 | 6433 | 380*380 | 128*128 | 2,97 | 3,60 | 24,0 | 4,75 | 1,68 |
| | Post | 4 | 6433 | 320*320 | 128*128 | 2,50 | 3,60 | 22,5 | 4,75 | 1,72 |
| 3 | Pre | 3 | 6433 | 400*400 | 128*128 | 3,13 | 3,60 | 24,0 | 4,75 | 1,68 |
| | Post | 4 | 7110 | 400*400 | 128*128 | 3,13 | 3,60 | 23,0 | 5,20 | 1,08 |
| 4 | Pre | 5 | 4850 | 350*350 | 128*128 | 2,73 | 3,60 | 25,0 | 3,58 | 1,10 |
| | Post | 5 | 5298 | 350*350 | 128*128 | 2,73 | 3,60 | 25,0 | 3,91 | 1,10 |
| 5 | Pre | 5 | 6813 | 320*320 | 128*128 | 2,50 | 3,60 | 25,0 | 5,03 | 1,72 |
| | Post | 5 | 6435 | 320*320 | 128*128 | 2,50 | 3,60 | 25,0 | 4,75 | 1,72 |

3.3 Software implementation

Software implementation was developed on Matlab R2012a[®] (The Math-Works, Inc., Natick, MA). ImageJ [26] and RadiAnt viewer [27] were auxiliary tools that were used to help visualizing image enhancement and defining regions of interest (ROIs).

The algorithm for perfusion quantification was implemented as a sequential set of steps, starting with the images from the dynamic acquisition and ending on the perfusion parameters determination. The flowchart of figure 3.4 indicates the major steps of the implemented algorithm.

The adopted strategy for calculating and displaying results was pixel mapping. This method gives perfusion information as maps spatially co-registered with the anatomical images on a pixel-by-pixel basis. Hence, a heterogenic appreciation of either the tumor regions or healthy parenchyma can be made, without losing information over the spatial variation of kinetic parameters, as it happens when considering a single ROI analysis.

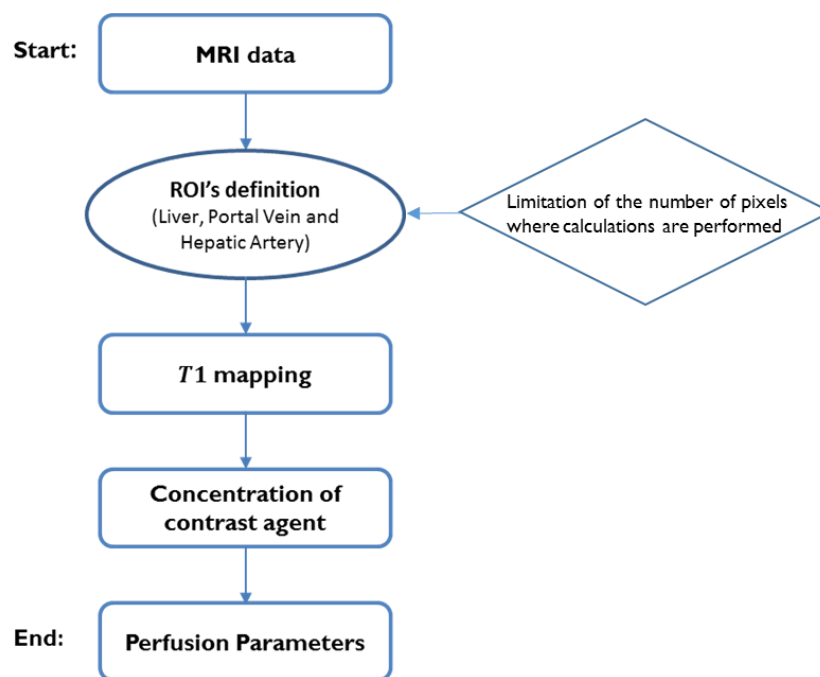


Figure 3.4: Flowchart illustrating the major steps of the algorithm that was implemented to estimate perfusion parameters on a pixel-by-pixel basis, using a dual-input one compartmental model.

3.3.1 ROIs definition

One of the objectives of this work was to compute perfusion parameters as parametric maps, in order to be able to assess the spatial variation of kinetic parameters. In order to optimize computation time, ImageJ was used to draw ROIs of the structures of interest: hepatic artery, portal vein and liver. These ROIs were saved and imported to Matlab as masks. Kinetic parameter calculation was only performed in pixels within the masks, thus discarding pixels in structures of non-interest and in the background noise.

It was necessary to determine 20 different ROIs of the liver for each patient, since each slice corresponds to different liver sections. Although ROI definition occurs with the data of a single dynamic and there are slight movements of the patient from dynamic to dynamic, the same ROIs were used in each of the fifty dynamics, thus assuming spatial correspondence over time. Although there are minor differences, these are minimized with the motion correction algorithm of the MR acquisition system.

Ideally, pre- and post-treatment acquisitions have the same geometry and cover the same slices. However, as can be observed from figure 3.5, in practice this situation does not happen and it was therefore necessary to define different ROIs for pre- and post-treatment.

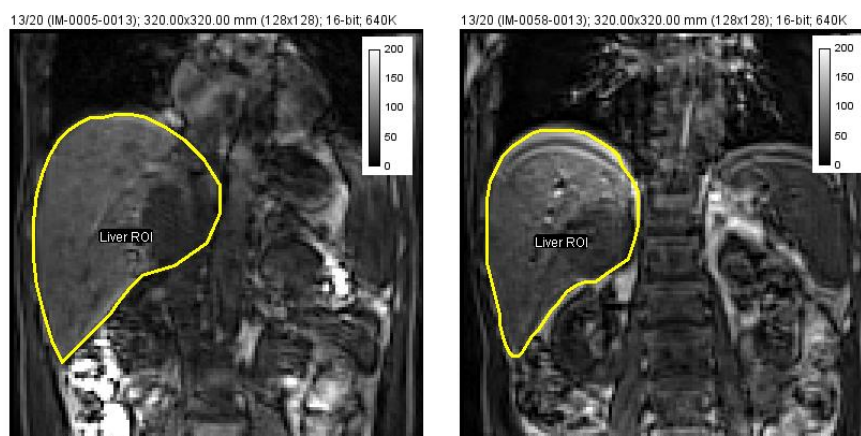


Figure 3.5: Liver ROIs of the same patient for the slice 13 drawn from the first temporal dynamic, corresponding to pre-treatment (left) and post-treatment (right). Differences in size, location and shape are highlighted.

For the blood vessels, a single ROI was determined (figure 3.6), corresponding to the slice that would capture the best representation of ‘in-plane’ flow in the vessel.

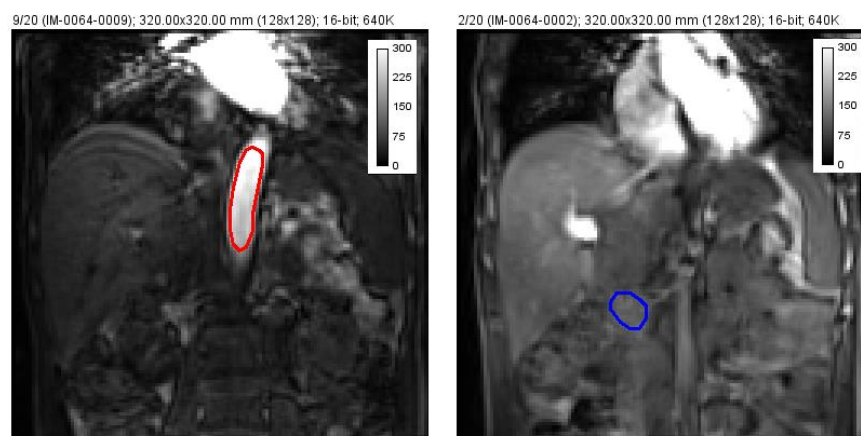


Figure 3.6: Abdominal aorta (red), used as substitute for the hepatic artery, and portal vein (blue) ROIs for the same patient.

It should be stressed that the abdominal aorta was used as a surrogate for the hepatic artery since the latter is often difficult to visualize and segment. It is considered that they are similar in both T_1 values and temporal variation of CA concentration.

Identification process of portal vein required the importation of the MRI data to Radiant viewer, which allowed the visualization of a fixed slice over the temporal dynamics and observe the contrast agent arrival to the liver. In order to precisely identify this structure, it was necessary to plot signal curves of pixels within the presumed ROI to confirm the existence of the enhancement peak after the baseline acquisitions.

3.3.2 $T1$ Mapping

The first step after the data has been corrected for motion is to determine the native $T1$ values of the tissues, i.e. performing $T1$ mapping. This is a necessary step to obtain parametric maps for the concentration of contrast agent for each dynamic acquisition. In order to perform $T1$ mapping, the variable flip angle method was applied. In this method, a series of $T1$ -weighted scans are acquired at different flip angles but keeping all remaining acquisition parameters constant. In this way, it is possible to determine the $T1$ value of tissues from the image contrast variation from scan to scan (figure 3.7).

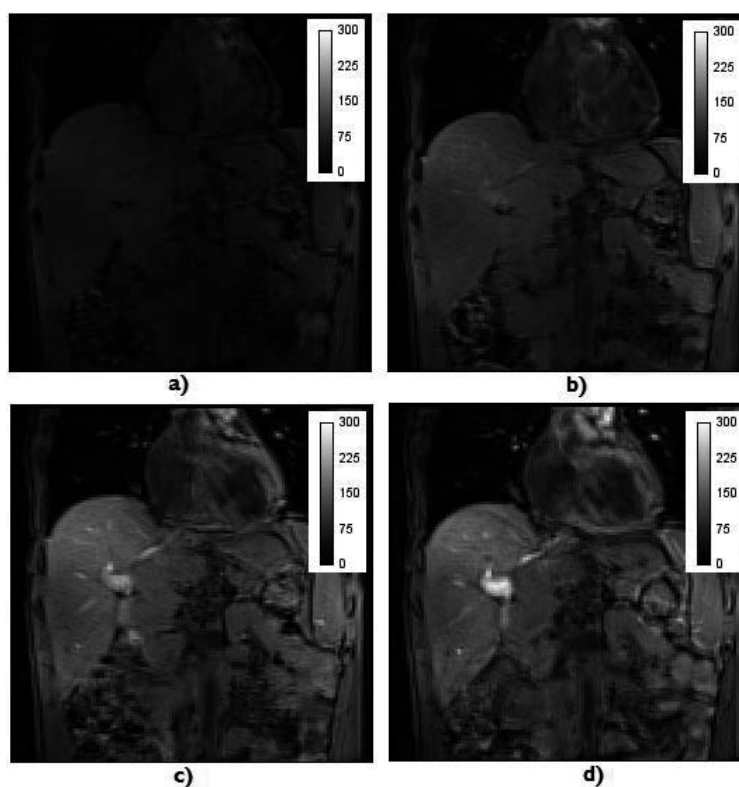


Figure 3.7: Different signal intensities from $T1$ -weighted images with variable flip angles. For $T1$ mapping 2° (a), 5° (b), 10° (c), and 15° (d) were used.

The signal intensity in $T1$ -weighted, considering a very small TE ($TE \ll T2^*$ approximation), for a given flip angle θ , and TR , is given by [28]:

$$S(\theta) = M_0 \sin(\theta) \frac{1 - e^{-TR/T1}}{1 - \cos(\theta)e^{-TR/T1}} \quad 3.5$$

Where $S(\theta)$ is the signal intensity for flip angle θ , M_0 represents the unknown longitudinal magnetization, and TR is the repetition time. Keeping TR constant, the signal intensity will only depend on $T1$ and θ . Let $a = e^{-\frac{TR}{T1}}$. In this case, equation 3.6 is rewritten as:

$$S(\theta) = M_0 \sin(\theta) \frac{1 - a}{1 - \cos(\theta) a} \quad 3.6$$

Further manipulations allow the linearization of 3.7 as:

$$\frac{S(\theta)}{\sin(\theta)} = a \frac{S(\theta)}{\tan(\theta)} + M_0(1 - a) \quad 3.7$$

Where the independent variable is $S(\theta)/\tan(\theta)$ is the independent variable and $S(\theta)/\sin(\theta)$ is the dependent variable. The $T1$ values are straightforwardly determined by a linear fit of eq. 3.8 to the experimental pairs of values $(S(\theta)/\tan(\theta), S(\theta)/\sin(\theta))$:

$$a = e^{-TR/T1} \Rightarrow T1 = -\frac{TR}{\ln(a)} \quad 3.8$$

Considering a curve of signal intensity as a function of the flip angle (figure 3.8), keeping TR constant, for a given $T1$, there is an optimal flip angle to obtain the maximum

signal after a series of excitation pulse, called the Ernst angle [28]. In order to obtain an accurate T_1 measurement it is important that the range of flip angles that are used in the measurements includes the Ernst angle (peak of the curve).

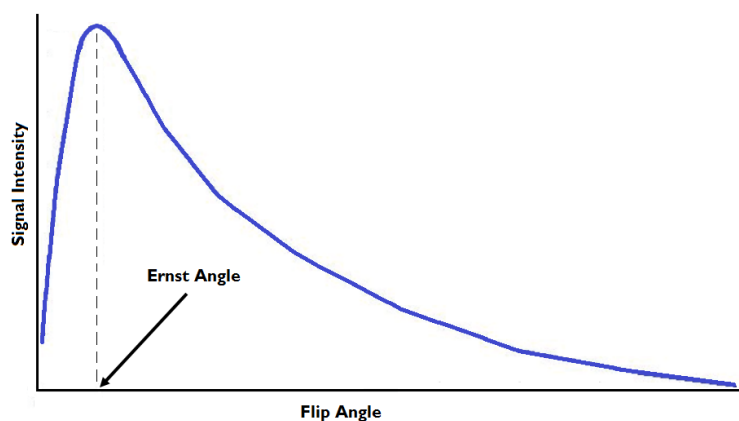


Figure 3.8: Dependence of the signal intensity on the flip angle. The peak of the curve corresponds to the Ernst angle. Based on [28].

3.3.3 Contrast agent concentration conversion

After the baseline T_1 for a particular pixel is known, it is possible to determine the contrast agent concentration that led to signal enhancement in that pixel. The paramagnetic properties of the contrast agent accelerate the longitudinal relaxation process, i.e. T_1 is shortened. In T_1 -weighted images the signal intensity is inversely proportional to T_1 and the relaxation rate increases proportionally to the concentration of CA [21] according to:

$$\frac{1}{T_1} = \frac{1}{T_{10}} + r_1 C \quad 3.9$$

Where r_1 is the relaxivity of the CA, a parameter that describes how T_1 changes in the presence of a certain concentration of CA. The relaxivity of Gadovist has the value of $3,58 \text{ L mmol}^{-1} \text{ s}^{-1}$ [29], and T_1 and T_{10} are respectively the T_1 values after and before contrast injection.

It was necessary to know how $T1$ varies over time depending on the concentration as a function of the variation of signal, i.e.:

$$T1(t, C(t)) = f\left(\frac{S(t)}{S(0)}\right) \quad 3.10$$

Considering both the signal before - $S(0)$ and after - $S(t)$ CA injection to be:

$$S(0) = M_0 \sin\theta \frac{1 - e^{-TR/T10}}{1 - \cos\theta e^{-TR/T10}} \quad 3.11$$

$$S(t) = M_0 \sin\theta \frac{1 - e^{-TR/T1}}{1 - \cos\theta e^{-TR/T1}} \quad 3.12$$

Their ratio is given by:

$$\begin{aligned} \frac{S(t)}{S(0)} &= M_0 \sin\theta \frac{1 - e^{-TR/T1}}{1 - \cos\theta e^{-TR/T1}} \\ &\times M_0 \sin\theta \frac{1 - \cos\theta e^{-TR/T10}}{1 - e^{-TR/T10}} \frac{1}{M_0 \sin\theta} \end{aligned} \quad 3.13$$

Considering $y = \frac{S(t)}{S(0)}$, $x = \frac{1 - \cos\theta e^{-TR/T10}}{1 - e^{-TR/T10}}$ and $a = e^{-TR/T1}$, the previous equation comes as:

$$y = \frac{1 - a}{1 - a \cdot \cos\theta} \times x \quad 3.14$$

Isolating the 'a' parameter:

$$a = \frac{x - y}{x - y \cos \theta} \quad 3.15$$

And substituting 'a':

$$e^{-TR/T1} = \frac{x - y}{x - y \cos \theta} \Leftrightarrow -\frac{TR}{T1} = \ln\left(\frac{x - y}{x - y \cos \theta}\right) \Leftrightarrow T1 = \frac{-TR}{\ln\left(\frac{x - y}{x - y \cos \theta}\right)} \quad 3.16$$

There are two separate equations for $T1$. Combining them it is possible to have concentration over time given by:

$$\frac{1}{\frac{1}{T_{10}} + r_1 C(t)} = \frac{-TR}{\ln\left(\frac{x - y}{x - y \cos \theta}\right)} \Leftrightarrow C(t) = \frac{1}{r_1} \left(\frac{-\ln\left(\frac{x - y}{x - y \cos \theta}\right)}{TR} - \frac{1}{T_{10}} \right) \quad 3.17$$

Substituting 'x' and 'y' in the equation, the concentration in (mM/L) is given by:

$$C(t) = \frac{1}{r_1} \left(\frac{-\ln\left(\frac{\frac{1 - \cos \theta e^{-TR/T10} - \frac{S(t)}{S(0)}}{1 - e^{-TR/T10}} - \frac{S(t)}{S(0)}}{\frac{1 - \cos \theta e^{-TR/T10} - \frac{S(t)}{S(0)}}{1 - e^{-TR/T10}} - \frac{S(t)}{S(0)} \cos \theta}\right)}{TR} - \frac{1}{T_{10}} \right) \quad 3.18$$

Observing equation 3.19, the concentration will only depend on known parameters: the temporal variation of the signal after contrast injection, the signal $S(0)$ before contrast injection, flip angle θ , relaxivity r_1 of the CA, repetition time TR and the $T1$ native values $T1_0$.

For the implementation of this method, the first step was to differentiate between the baseline signal from the one acquired after contrast injection. A ROI was plotted in an artery, usually the abdominal aorta, with in-plane flow and the signal intensity variation over time was used to identify the baseline more accurately. Selecting a pixel (figure 3.9a) it is possible from its signal temporal variation plot (figure 3.9b) to identify, for this patient, 3 points belonging to the baseline.

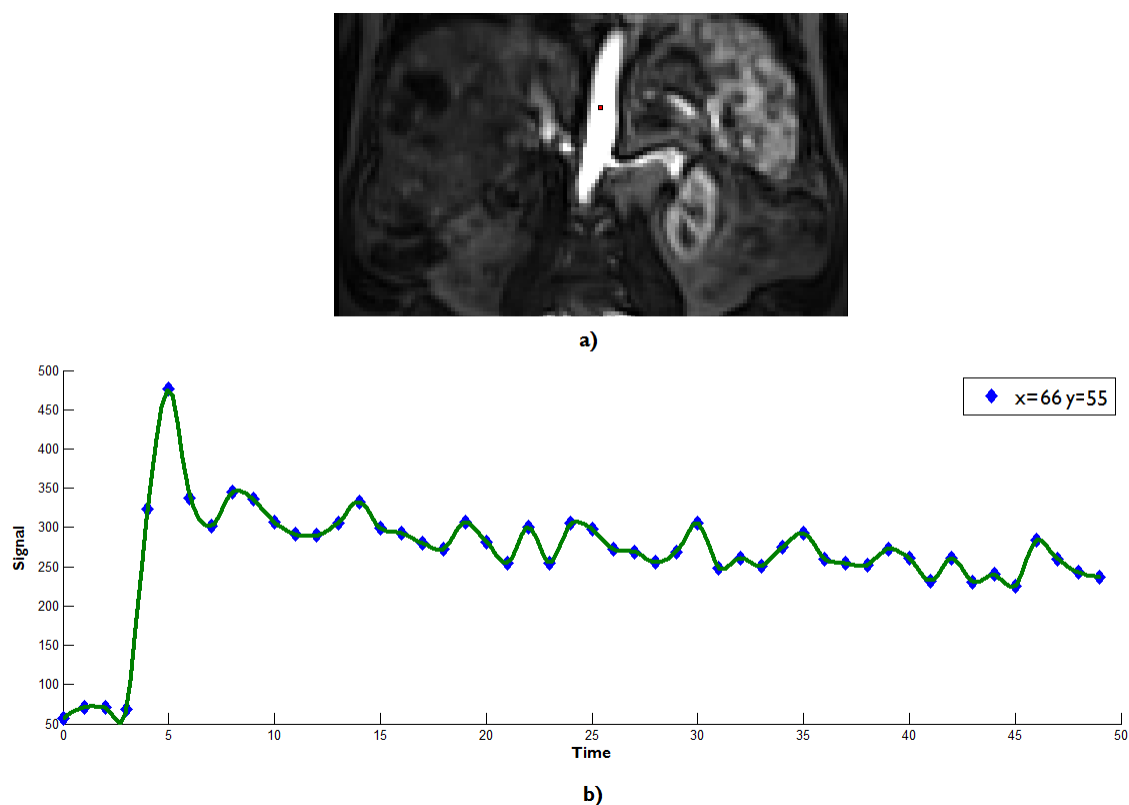


Figure 3.9: a) Anatomical location of the chosen pixel in the artery region. b) Temporal variation of the signal over time (arbitrary units). Identification of a baseline of 3, starting the acquisition at time 4.

The baseline had to be identified for each patient, and for pre- and post-treatment data, since the baseline length varied from patient to patient and even within

patient. The signal intensity $S(0)$ in equation 3.18 was determined, for each pixel, from the average signal intensity of the baseline.

Having determined the baseline signal $S(0)$, the signal variation over time $S(t)$, the native $T1$ values, and knowing the relaxivity of the contrast agent and the acquisition parameters TR and θ , it is possible to apply 3.18 to convert signal intensity variation to CA concentration variation.

3.3.4 Perfusion Parameters

After the signal to contrast agent concentration conversion has been made, the same procedure is applied for the portal vein and hepatic artery ROIs. Both $T1$ and concentration determination for these structures were performed in a pixel-by-pixel basis. Although for the kinetic parameters simulation, according to the model, each pixel within the liver ROI is defined by a set of parameters that is used to perform the non-linear fit. For each pixel there is the contrast agent concentration curve of that position, and single hepatic artery and portal vein curves. Both hepatic artery and portal vein concentration curves were obtained by averaging the values within the region of the respective ROIs. In other words, the concentration of either one of the vessels, for a temporal instant, is represented by a single average value that is the same for any pixel of the liver in the same temporal instant.

At this point, having determined the liver concentration maps, and the portal vein and hepatic artery input functions, it is possible to apply the dual-input one-compartment model equation 3.1 to extract the physiological kinetic constants k_{1a} , k_{1p} and k_2 to former conversation into perfusion parameters.

Solving the equation 3.1 for $C_L(t)$ and taking into account the transit time from the hepatic artery and portal vein to the liver by adding the τ_a and τ_p delay parameters, the concentration of contrast agent over time is

$$C_L(t) = \int_0^t [k_{1a}C_a(t' - \tau_a) + k_{1p}C_p(t' - \tau_p)]e^{-k_2(t-t')}dt' \quad 3.19$$

Where t' represents a dummy integration variable and $C_L(0) = 0$. Knowing the temporal variation of contrast agent concentration in the liver and in both the hepatic artery and the portal vein, it is possible to calculate, the unknown kinetic parameters k_{1a} , k_{1p} and k_2 , using a non-linear fitting algorithm.

Because the mean transit times from the aorta and portal vein regions to the liver ROI, respectively represented by the delay parameters τ_a and τ_p vary depending on the patient and how its concrete measurement was performed during acquisition, was assigned a value of 3 seconds for both [30].

The Levenberg-Marquart was the chosen method for the non-linear fit of the kinetic parameters to the data by the equation 3.20. This method is suitable to use when fitting a parameterized function to a set of measured data points by minimizing the sum of the squares of the errors between the data points and the function, where there is a non-linear dependence on the unknown parameters [31].

The implementation of this method comprises an iterative procedure where the values of the unknowns (in our case the kinetic constants) are adjusted in order to minimize the sum of the squares of the errors between the values predicted by the model and the measured data.

3.3.5 Implementation in Matlab

Matlab scripts were created to implement each step of the algorithm.

For the determination of the $T1$ values, the software proceeds as follows:

1. Starts a cycle that reads the dicom images corresponding to all the flip angles and stores the values in a multidimensional array of size $nx \times ny \times z$, where nx and ny correspond to the number of pixels in the vertical and horizontal directions, and z stands for the number of flip angles.
2. Extracts TR and flip angle values from the dicom header and creates a flip angle vector $([\theta_1 \theta_2 \theta_3 \dots \theta_z])$ where each θ corresponds to the specific value of the flip angle.
3. Runs a double cycle that goes through all nx and ny indexes and for each pixel extracts the signal values of each flip angle acquisition and stores into a vector $([S_1 S_2 S_3 \dots S_z])$ of the same size of the flip angle. With the TR , flip angle and signal vectors uses the *polyfit* function, in order to find the coefficients of the polynomial $P(X)$ of degree 1 that best fits equation 3.7 in a least-squares sense and on a pixel-by-pixel basis.
4. Repeats of the previous process to all the slices, to obtain 20 dicom images containing the parametric maps of the native $T1$ values of the tissues.

After $T1$ mapping being completed, in order to achieve the CA concentration, the script goes through the following steps:

1. Receives the directories of $S(0)$, $S(t)$ and $T1$ and imports its values to the workspace.
2. Uses the dicom header of the dynamic scans to extract TR and θ parameters.
5. Based on the number of dynamic scans, creates a multidimensional array of size $nx \times ny \times N$ where nx and ny correspond to the number of pixels in the vertical and horizontal directions and N stands for the number of dynamics.
3. Initiates a cycle that goes through all nx and ny indexes of the array and for each position extracts the value from $S(0)$, $S(t)$ and $T1$ for that position. $S(t)$ is here a vector of size $1 \times 1 \times N$ containing all values of signal intensity for that specific pixel. Applies the 3.18 formula to these values and repeats the process for all image indexes and sets the concentration values, obtained also as vector, in the multidimensional array position (x_i, y_i) .
4. Repeats the process to all slices.

The resulting output consists of a multidimensional array (figure 3.10) where each 2D array corresponds to a map of contrast agent concentration at a given time.

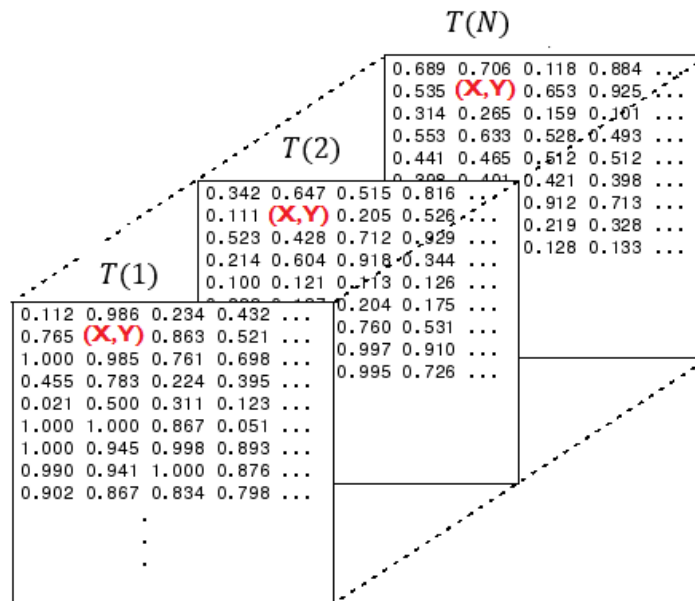


Figure 3.10: Example (with non-real values) of the type of structure obtained in the calculation of concentration. Choosing a pixel of coordinates (X, Y) , it is possible to access the values of concentration over time (represented by the third dimension). Adapted from [36].

The previous steps were applied to pixels within the liver ROI but, in order to determine the kinetic constants referred to in equation 3.19, $T1$ and contrast agent concentration of the hepatic artery and portal vein had to be determined. $T1$ calculation was performed pixel-by-pixel at the defined ROIs for the blood vessels, but only a single value was considered, corresponding to an average of the $T1$ values inside the region. Only values between 900-2000 milliseconds were accepted and in cases where the average values were outside the range, $T1$ was artificially set in 1584 milliseconds for the portal vein and 1664 milliseconds for the hepatic artery, values estimated for the longitudinal relaxation of blood at 3T [32]. Same procedure was made for the contrast agent concentration determination at the blood vessels, where only one value for each instant of the dynamic study was determined, corresponding to the average values for the concentration at the hepatic artery and portal vein ROIs.

Having determined the concentration of the contrast agent in all structures comprised in the model, it is possible to simulate the kinetic constants and calculate the perfusion parameters.

The implemented method for the perfusion parameters determination goes through the following steps:

1. Receives the directories of C_L , C_a and C_p and imports its values to the workspace.
2. Uses the dicom header of the dynamic scans to create a vector of times, correspondent to the real acquisition times.
3. Creates an objective-function from equation 3.19 to simulate the liver contrast agent concentration, implemented by the *cumtrapz* function that computes an approximation of the cumulative integral of $C_L(t)$ via the trapezoidal method.
4. Loads the liver ROIs to the workspace as masks to limit the number of pixels used in the computations of the next step.
5. Initiates a cycle that goes through all nx and ny indexes of the liver concentration multidimensional array (being nx , ny , and N , the number of pixels in the vertical and horizontal directions, and the number of dynamics, respectively). For each index correspondent to the liver mask, gets $C_L(t)$, $C_a(t)$, and $C_p(t)$ values as vectors of size $1 \times 1 \times N$ containing all temporal values of contrast agent concentration for that specific pixel. Applies the Levenberg-Marquardt algorithm through the *lsqnonlin* Matlab fitting function to the objective-function iterates until the sum of the squares of errors between the parameterized objective-function and the experimental curve obtained for C_L is minimized with a maximum of 800 iterations.
6. From the fitted curve $C_L(t)$ derives the set of kinetic constants used in the equations 3.2, 3.3 and 3.4 to determine the perfusion parameters P_a , P_p and P_L with the extraction fraction equal to 1.
7. Repeats the process for all indexes and set the determined values in four parametric maps that are converted to dicom images.
8. Repeats the process to all slices.

Chapter 4

Results

4.1 Signal Enhancement and and tumor identification

Figure 4.1 presents a typical example of coronal abdominal slice acquired during the dynamic study. The data belongs to Patient 3 and was acquired during the post-treatment examination. This example illustrates the expected signal enhancement after contrast injection at different time points.

Figure 4.1a was acquired before contrast injection and it shows the baseline signal from tissues. A few seconds after CA injection (figure 4.1b), there is signal enhancement at the bottom of the right liver lobe, indicating the tumor location. In addition, regions such as the heart or arteries also shown signal enhancement. Figure 4.1c represents the signal from the last dynamic that was acquired for the same slice. It shows contrast wash-out in the tumor while healthy liver parenchyma still shown signal enhancement.

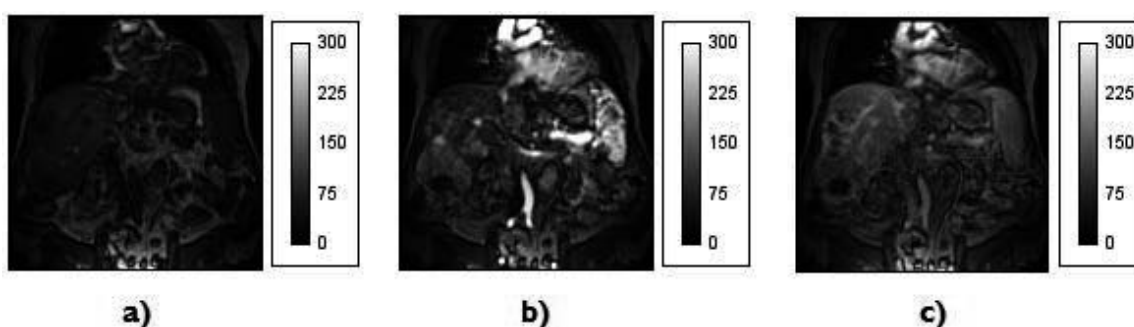


Figure 4.1: Contrast-enhancement in a liver MR slice from post-treatment acquisition of patient 3: a) pre-contrast; b) "early" contrast-enhancement; c) "late" contrast-enhancement.

Signal enhancement of the liver parenchyma is lower compared to the enhancement of the hypervascularized area, where there is higher concentration of contrast between the plasma and the tumor region. These results are expected as tumor

has an earlier enhancement as it is mainly fed by arteries, while the blood input of the normal parenchyma is from the portal vein. From figure 4.1b, a representative pixel from both tumor and healthy parenchyma regions were chosen and their variation of the signal intensities over time was plotted (figure 4.2) in order to see enhancement differences.

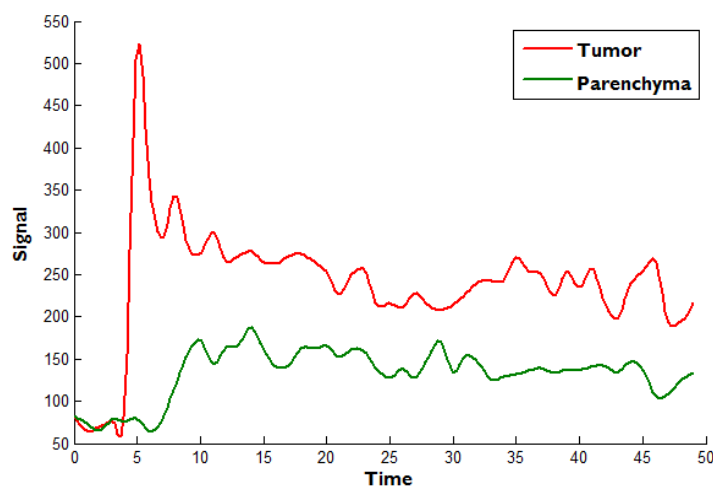


Figure 4.2: Typical enhancement signal curves (of arbitrary units) derived from pixels in the tumor and healthy parenchyma regions respectively.

From figure 4.2 it is possible to notice the existence of an enhancement peak, correspondent to the signal from early dynamics of the tumor location with progressive washout over time. For the pixel from the healthy parenchyma it is possible to see that there is also latter signal enhancement with smaller magnitude, when compared to the one from the tumor. The latter and smaller enhancement from parenchyma ROIs and the early raising in signal enhancement from tumor ROIs are characteristic behaviors from both regions.

In this way, the identification of the tumor region and boundaries from the first 3 dynamic after contrast injection is, in general, quite straightforward. Images from the last dynamics are not suitable as they show the late contrast-enhancement of normal liver parenchyma while the tumor is already in the wash-out phase. As a consequence, the identification of the tumor is less obvious in these dynamics.

4.2 ROIs definition

ROIs for liver, tumor, abdominal aorta and portal vein were defined in ImageJ. This tool was used instead of Matlab as it enables importation of all slices of each dynamic in a single stack, allowing very simple manipulation of the image brightness, contrast, color maps, drawing tools, among others functions. Given that ROIs from ImageJ were obtained in the *.roi* extension, a function to import the defined ROIs to the Matlab workspace was created. It transformed the defined ROI into a *.mat* file with values of 0's and 1's, masking the pixels within the ROI into values of 1.

The figures below show the ROIs for the liver (yellow) and for the tumor (magenta), corresponding with each patient. For each patient two sets of ROIs, corresponding with the acquisitions from pre- and post-treatment. Ideally, the same ROI for pre- and post-treatment analysis should be used. However, this approach could not be taken because the FOV in pre- and post-treatment acquisitions was often not positioned in exactly the same place. As a consequence, this led to changes in the position and orientation of the liver. Furthermore, the anatomy surrounding the tumor was often changed from pre- to post-treatment, which further complicated the process. In order to overcome this difficulty, the ROIs of pre- post-treatment were selected so that they would be positioned in approximately the same anatomical region.

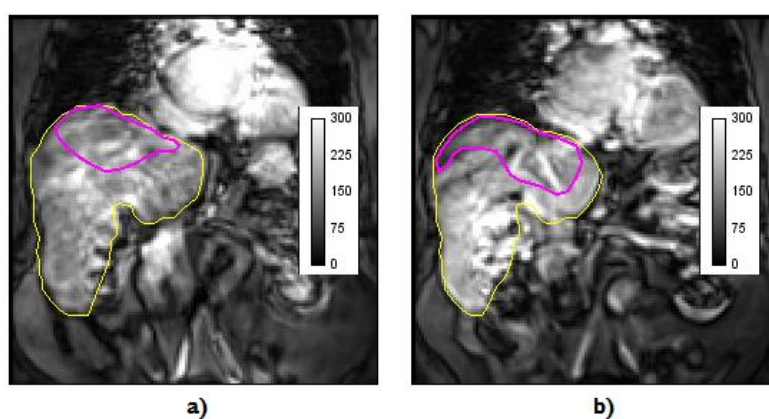


Figure 4.3: Liver (yellow) and tumor (magenta) ROIs of Patient 1 in: a) pre-treatment and b) post-treatment scans.

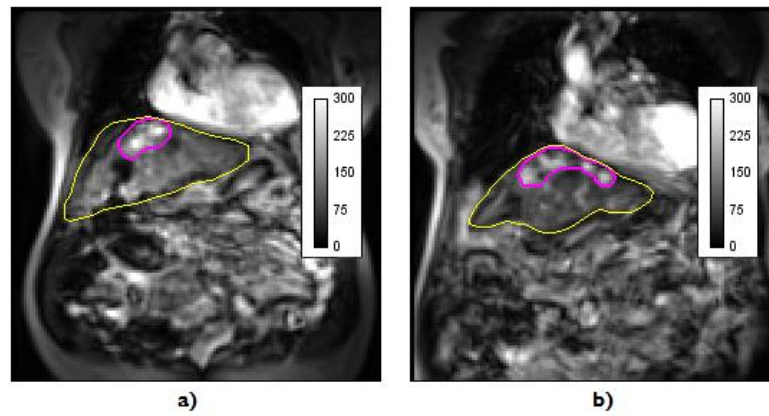


Figure 4.4: Liver (yellow) and tumor (magenta) ROIs of Patient 2 in: a) pre-treatment and b) post-treatment scans.

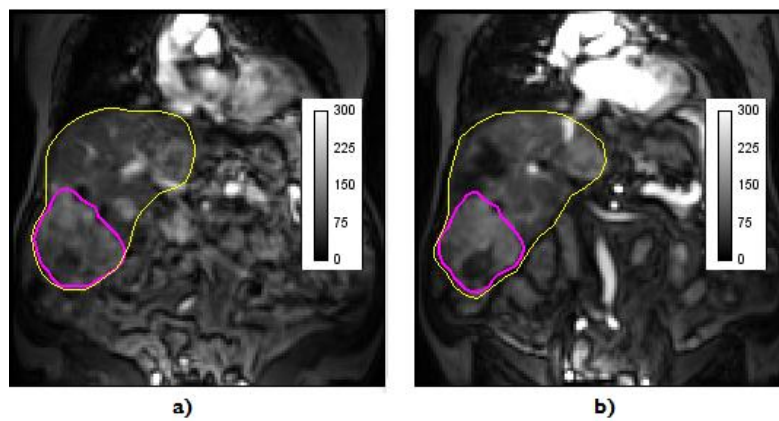


Figure 4.5: Liver (yellow) and tumor (magenta) ROIs of Patient 3 in: a) pre-treatment and b) post-treatment scans.

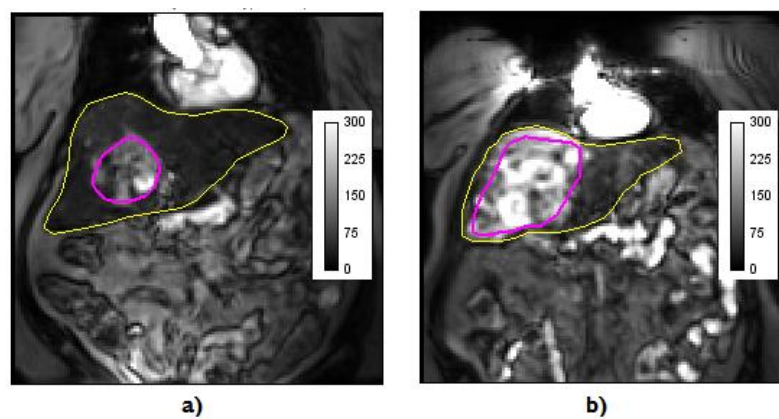


Figure 4.6: Liver (yellow) and tumor (magenta) ROIs of Patient 4 in: a) pre-treatment and b) post-treatment scans.

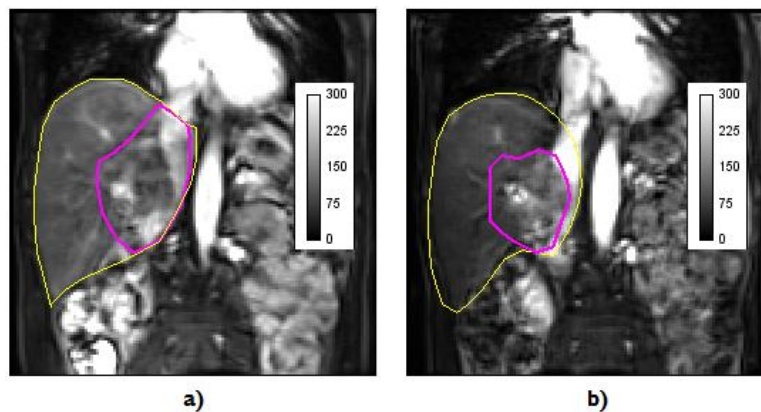


Figure 4.7: Liver (yellow) and tumor (magenta) ROIs of Patient 5 in: a) pre-treatment and b) post-treatment scans.

It is important to refer that in order to more accurately segment the tumor, which is often irregular and distributed amongst different slices, the defined ROIs are three dimensional, therefore defined with more than one slice.

4.3 *T1 parametric maps*

$T1$ parametric maps (PM) were obtained for all slices of every patient using the variable flip angle approach. Figures. 4.8-4.12 show the $T1$ PM of one slice per patient, the one where the tumor is more visible. $T1$ values are shown in milliseconds for pre-treatment (left) and post-treatment (right).

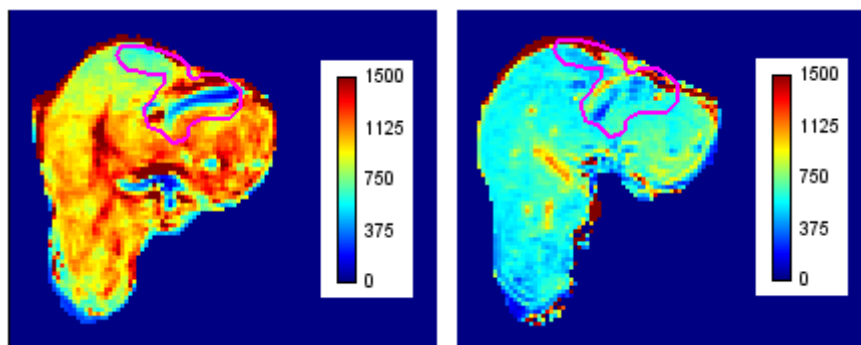


Figure 4.8: $T1$ parametric maps for Patient 1.

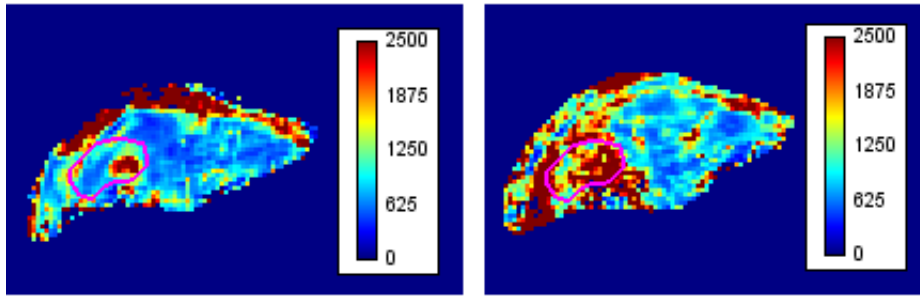


Figure 4.9: T_1 parametric maps for Patient 2.

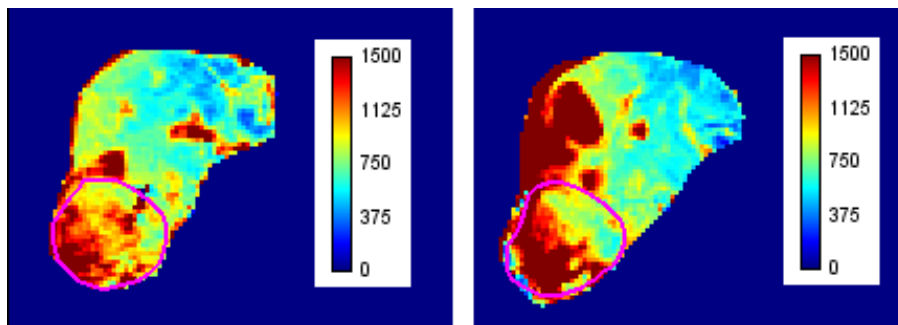


Figure 4.10: T_1 parametric maps for Patient 3.

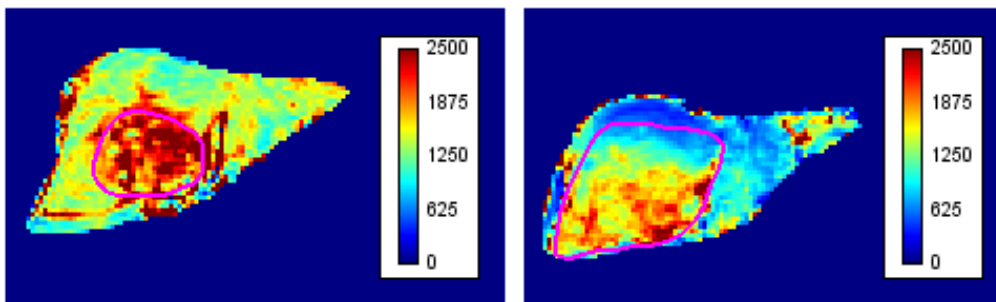


Figure 4.11: T_1 parametric maps for Patient 4.

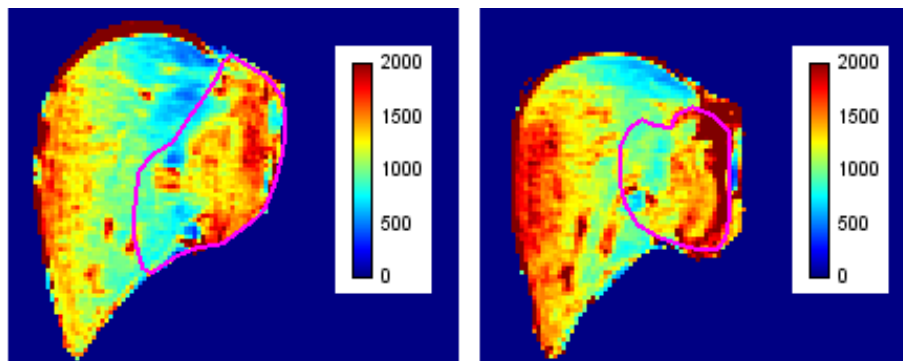


Figure 4.12: T_1 parametric maps for Patient 5.

Results demonstrate that, for all subjects, the highest $T1$ values are obtained in blood vessels and tumor regions. For example, for Patient 5 (figure 4.12) in pre-treatment (left), values in the range of 1500 – 1800 ms are positioned in the left lobe, which was previously defined as the tumor zone. As there is an increased inflow of arterial blood to the tumor zone, it is expected for these structures to have $T1$ values from approximately 1500 to 1700 ms , which correspond to the values of longitudinal relaxation of blood in a magnetic field intensity of 3T. In the same figure, the central part of the liver presents $T1$ values between 600 – 800 ms , which are characteristic values for hepatic parenchyma with normal perfusion. Apart from the area identified as a tumor, it is also possible to observe a region located in the right lobe, which also shows high values of $T1$, similar to those found in tumor. In the post-treatment $T1$ map of the same patient, an overall increase of $T1$ values can be seen, possibly suggesting tumor growth.

Another illustrative case is that of Patient 4, which is presented in figure 4.11. Here, the regional decrease in $T1$ values on post-treatment could suggest tumor regression. However, this result goes against what was shown in figure 4.6b, where there is a larger hepatic area of signal enhancement in post-treatment, thus suggesting the opposite, namely, tumor increase. This can be justified by the slice that was used to show the $T1$ map. Choosing another representative slice of the liver for the same patient in post-treatment (figure 4.13), it is observed that there is an increase of the area with high values of $T1$.

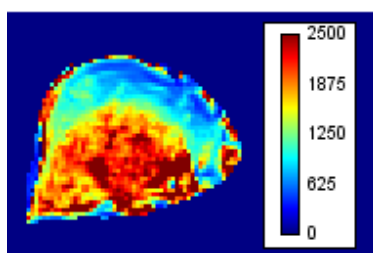


Figure 4.13: $T1$ map of an alternative slice of Patient 4 in post-treatment examination that shows a larger area of the liver with high $T1$ values.

For the remaining patients, a similar behavior of the spatial distribution of $T1$ values was observed, i.e. highest values of $T1$ corresponding with either tumor, largely

irrigated areas or blood vessels. The exception holds for Patient 1 (fig. 4.8) where there is a general increase of T_1 values from pre- to post-treatment maps.

4.3 Contrast Agent Concentration

It is possible to describe the evolution of CA concentration in tissues by converting the MR signal into concentration units (mM/L). Contrast agent concentration, an intermediate step in the algorithm to calculate kinetic parameters, was stored in a multidimensional array. Thus, for each slice there is a $n_x \times n_y \times N$ array where the concentration values for each dynamic can be represented as a 2D 128×128 matrix of doubles. By storing the CA concentration in a multi-dimensional array, it is possible to plot CA concentration-time curves on a pixel-by-pixel basis, by choosing pixels from desired regions. This procedure is illustrated in figure 4.14.

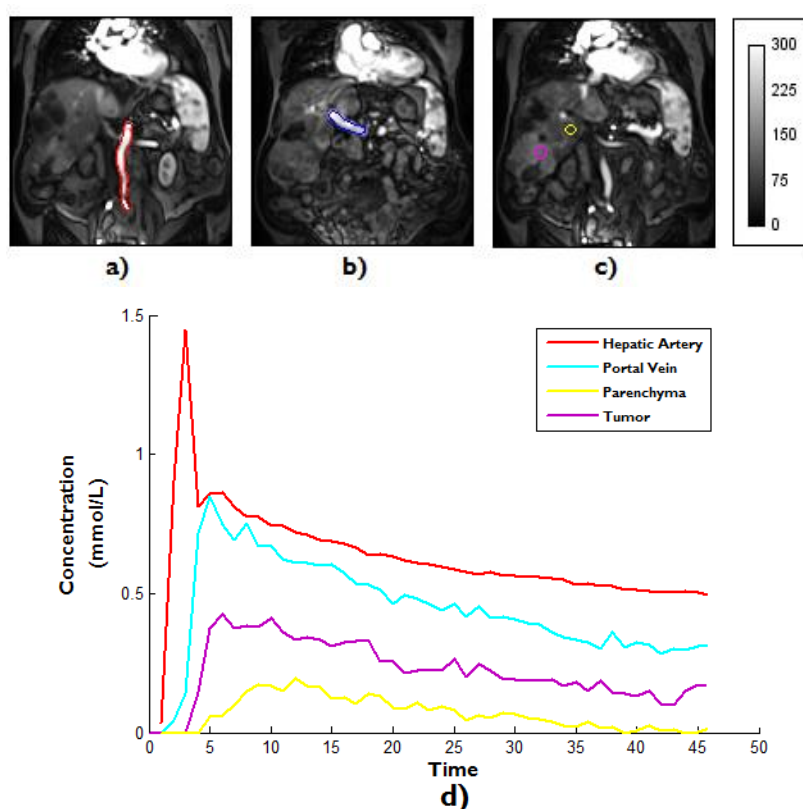


Figure 4.14: a) to c) - Identification of the abdominal aorta), portal vein and small segments from tumor and parenchyma ROIs from post-treatment dynamics of Patient 3. d) Average CA concentration-time curves from the displayed ROIs.

The tumor shows a rapid increase in CA concentration, when compared to the behavior of healthy parenchyma, followed by a quick washout, which reflects the fact that the tumor is a highly irrigated region.

Furthermore, the abdominal aorta and the portal vein concentration-time curves show the expected relative peak time delay, i.e. the peak of CA concentration is reached first in the artery and then in the portal vein. As expected, there is a rapid and greater accumulation of contrast in the tumor ROI compared to the parenchyma. This is a result of the increased local arterial blood feeding the tumor when compared to the healthy parenchyma, where a main portal vein blood feeding is expected.

Similar concentration curves were obtained for the other patients using other sets of pixels. The concentration curves in each pixel were used to calculate the kinetic parameters using a non-linear fitting procedure.

4.4 Perfusion Parameters

Figures 4.15 – 4.19 show the kinetic parametric maps obtained before and after treatment for all patients, considering the dual-input one-compartment model. It was chosen to present as final results the kinetic constants (k_{1a} , k_{1p} , k_2) and the overall liver perfusion (PL), calculated according to equation 3.4. The kinetic parameters are presented in units of s^{-1} as well as the liver perfusion. The extraction fraction of the contrast agent in the liver, E has no units and in this work it was assumed to be 1 for all cases. In order to present the results in DICOM images, it was necessary to apply a scaling factor of 10^4 to all values, so that real values can be obtained from the integers stored in DICOM format, divided by the scaling factor.

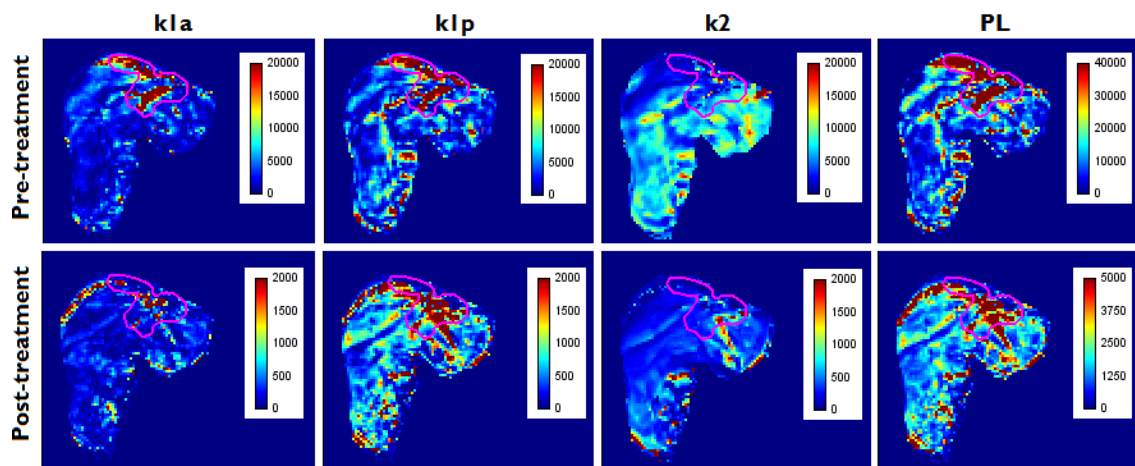


Figure 4.15: k_{1a} , k_{1p} , k_2 and PL parametric maps for Patient 1.

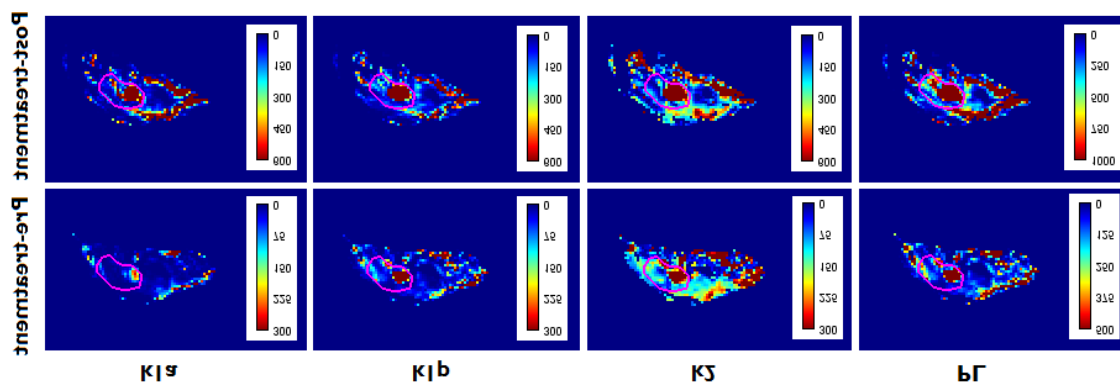


Figure 4.16: k_{1a} , k_{1p} , k_2 and PL parametric maps for Patient 2.

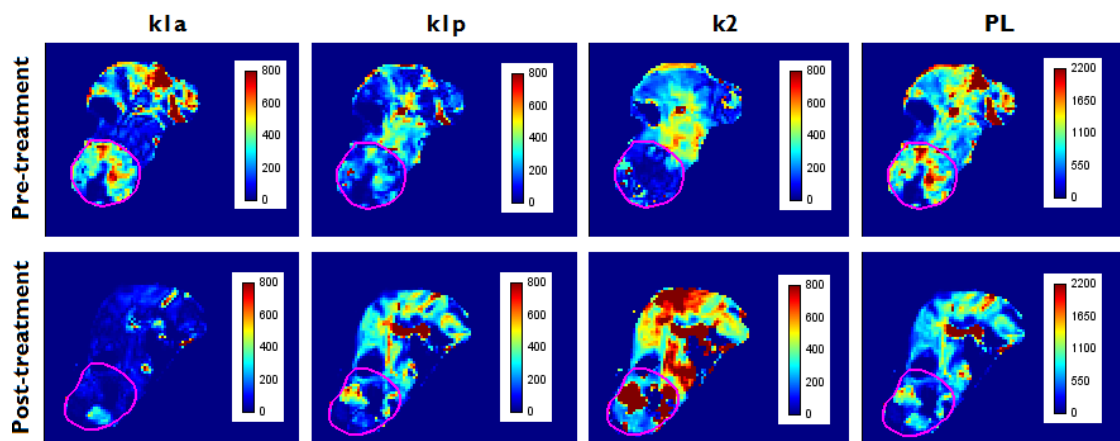


Figure 4.17: k_{1a} , k_{1p} , k_2 and PL parametric maps for Patient 3.

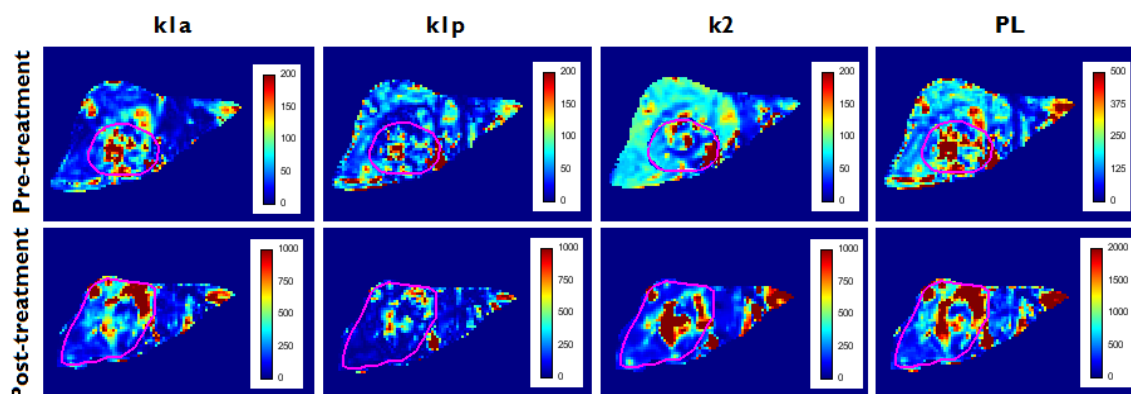


Figure 4.18: k_{1a} , k_{1p} , k_2 and PL parametric maps for Patient 4.

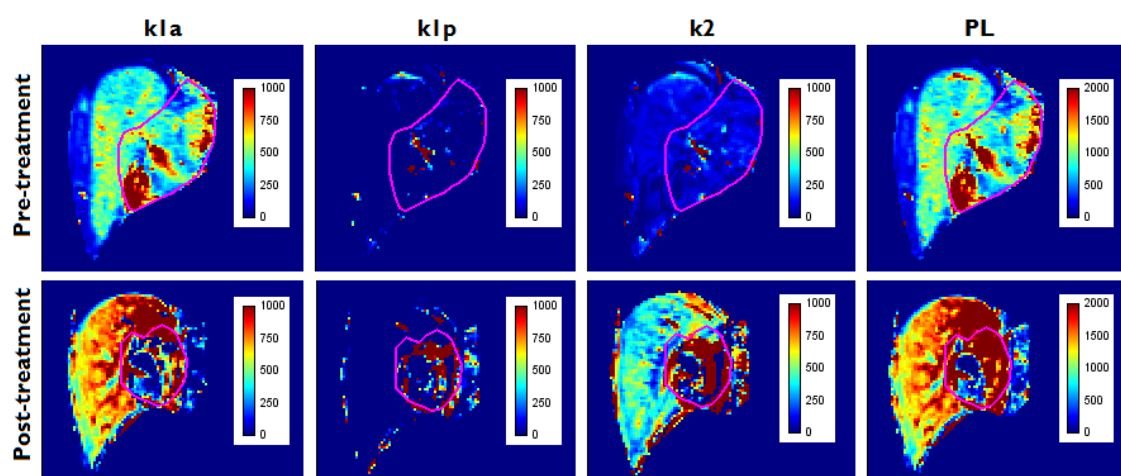


Figure 4.19: k_{1a} , k_{1p} , k_2 and PL parametric maps for Patient 5.

The success treatment of patients may be assessed qualitatively by comparing the perfusion status before and after treatment. According to the proposed model, it is possible to classify patients into categories of treatment responders and non-responders. Response to treatment implies an overall decrease in perfusion in the post-treatment PL parametric maps, which was found in Patient 1 and Patient 3. Patients 2, 4 and 5 are accordingly to this model non-responders since there is an increase in the overall perfusion after treatment.

Even through visualization of the images of early signal enhancement, tumor boundaries were not easy to define for Patient 1. In the signal intensity images, no localized signal enhancement occurs, in fact, dispersion of high values of intensity are observed among the entire region of left lobe and in the upper zone of the right lobe.

Using the same ROI and analyzing the parametric maps from the same slice before and after treatment, there is a significant decrease in all kinetic parameters and consequently in the global perfusion. It is important to refer that pre-treatment maps present a range of values 8 times superior that the post-treatment ones.

k_{1a} and k_{1p} maps of Patient 2 after treatment show increased values when compared to the same parameters before treatment, resulting in an overall increase in liver perfusion. Increased values of perfusion on the liver outer edges may suggest new vessels recruitment and consequently tumor growth despite treatment. Although this effect may also be artifactual. It is noticed that there are many areas of the liver where perfusion is zero. Furthermore, k_2 maps present higher values than k_{1a} and k_{1p} for this patient, suggesting high rates of contrast agent extraction from the liver by the hepatic vein.

Besides the defined ROI of the tumor for Patient 3, it is possible to identify, in figure 4.17, other tumoral masses in the upper region of the liver, which also have increased kinetic constants and overall perfusion. From the comparison of the color maps before and after treatment it becomes evident that there is an overall decrease of the liver perfusion after 3 months of treatment. An interesting observation in this patient is the existence of an area within the defined ROI for the tumor, where all parameters are zero. The absence of blood perfusion in this region may suggest the presence of a necrotic area. Comparing k_{1a} and k_{1p} maps before treatment, it is possible to find alterations of the vascular supply of the liver. Here the blood supply to the tumor is mainly arterial. However, from the observation of the post-treatment maps, seems to be a reestablishment of the blood supply, expected to be mainly from the portal vein, by the decrease in k_{1a} values and increase in the k_{1p} ones.

From the parametric maps of Patient 4, in figure 4.18, it is possible to see augmented liver perfusion after treatment. In both pre- and post-treatment maps, the contribution of global liver perfusion seems to be mainly arterial since the values of k_{1a} rate constant are relatively higher than k_{1p} ones. Besides the increase of the perfusion, there is tumor migration to an upper region from its previous location.

Parametric maps of the Patient 5, illustrated in figure 4.19 show a marked increased liver perfusion after treatment. Apart from the highest values of perfusion being found within the ROI defined for the tumor, it is possible to see increased blood perfusion also for the hepatic parenchyma surrounding the tumor. This may represent the process of recruitment of more vessels to the tumor region, supplied by the hepatic artery through neoarteriogenesis process. In fact, there is almost no blood supply contribution from the portal vein to the tumor. It is possible to see that there are high values of k_{1p} in few points within the tumor, being mainly zero for the rest of the liver. Within the tumor of the post-treatment parametric maps, it is possible to see a small area with absence of perfusion, suggesting development of necrotic tissue.

Chapter 5

Discussion

The main goal of the present work was the implementation of a software for perfusion quantification in liver that better reflected the real liver blood supply. A dual input one-compartment model was considered, comprising both venous and arterial blood contributions to the liver. Using this mathematical model it was possible to determine the temporal evolution of the contrast agent concentration and calculate the kinetic parameters that described the transport of the contrast agent from the portal vein and hepatic artery to the liver.

For that purpose, an algorithm composed by a series of distinct steps was implemented. The software implementation was not a trivial procedure as it involved the manipulation of complex numeric methods, handling several variables and non-linear equations. Several strategies were adopted during the implementing procedure, in order to keep model integrity and to obtain a software with suitable clinical applicability.

One of the adopted strategies was the minimization of the total computation time with a view on clinical application. As already mentioned, the number of pixels that were used in the calculations was limited only to the structures of interest. For that purpose, ROIs limited to the liver and few adjacent structures were defined. This procedure was particularly important for the calculation of the native $T1$ values as well as that of the kinetic parameters, since these operations involve non-linear fitting procedures, which have long computation times. With the application of ROIs, the computation time decreased considerably (from approximately two hours to twenty minutes per patient, for the kinetic parameters determination procedure). Some difficulties were found in the identification of anatomical structures, especially in the case of tumor, portal vein and liver edge. The liver is a large organ and is therefore susceptible to motion artifacts and partial volume effects, hence making the identification of liver

boundaries sometimes hard. Furthermore, tumors are irregular structures that vary their position depending on the imaging slice. For that reason, tumor ROIs were defined not only based on a single slice, but considering other slices that included parts of the same tumor, i.e., 3-dimensional ROIs. The portal vein was the most difficult structure to identify because of its size and because sometimes it was positioned in an oblique plane to the acquisition plane.

Another assumption consisted on the arterial input function measurement in the abdominal aorta, instead of measuring it on the hepatic artery. The proposed model required the definition of both an arterial and venous input functions. There were no problems in detecting the venous function, which was acquired over the portal vein ROI. However the arterial input function definition, which ideally would be acquired over the hepatic artery, was more difficult. The identification of this structure was practically impossible due to its reduced size and position within the FOV, so a ROI over the abdominal aorta was placed, assuming that both arteries had the same signal and consequently the same contrast agent concentration.

The removal of outliers was one of the strategies that was used to keep model integrity and avoid the propagation of numerical instabilities. Depending on the orientation of the portal vein and abdominal aorta with respect to the FOV, it could be that the flow in these vessels was not completely in-plane. As a consequence, inflow effects originated native $T1$ values outside the expected range of values for the longitudinal relaxation of blood at 3T. This represented a potential source of error to the contrast agent concentration curves of the blood vessels. In order to minimize this effect, it was chosen to attribute $T1$ values from literature to those pixels that were affected by inflow effects. It was also necessary to remove outlier values when calculating the contrast agent concentration for the liver. In this procedure it was noticed the presence of negative values of concentration. Spatial localization of these pixels suggested that they were either from noisy regions or from regions with no contrast enhancement and it was chosen to set the contrast agent concentration values of these pixels artificially to 0. The justification for these outlier values reflects one of the major limitations of this work, in which all model equations were equally applied to every pixel, regardless of whether there was signal enhancement from contrast agent arrival or not.

Pixels that violated the model assumption of enhancement affected the final results and were a confounding factor in the interpretation of kinetic parametric maps. For that reason, they had to be signaled as outliers.

One important point consisted in the assignment of values to parameters of the model equations, which were unknown or for which no measurements were made. The values of the mean transit time of the contrast agent from hepatic artery and portal vein to the liver were considered to be, for both parameters, equal to 3 seconds. This value was taken from literature, and it is not considered a potential source of error, as it is nearly half of the temporal resolution that was used in the acquisition of the data. In this situation, the transport of the contrast agent from the abdominal aorta and portal vein to the liver can be considered to be instantaneous. Ideally, the correct assessment of the perfusion parameters also takes into account the influence of the small vessel hematocrit and the correct measurement of the extraction fraction of the contrast agent in the liver, which did not occur. The hematocrit measurement represents an invasive procedure that could not be performed for all patients, and for the calculations, its influence was discarded. Due to the lack of extraction fraction measurement, it was considered to be 1, as this value is referenced by literature to be used in situations where the contrast agent has free access to the extravascular space. These two last assumptions may have caused an underestimation of the rate constants and consequently of the overall liver perfusion.

The validation of the software using a clinical population with HCC allowed to highlight the positive aspects of the dual-input one-compartment model analysis of the data over the traditionally used model. The parametric maps, show many differences between k_{1a} and k_{1p} constants, which proves distinct contributions for the overall liver perfusion from arterial and venous input. This is a very important issue when considering the Tofts model that only assesses perfusion through the determination of the K^{trans} and considering a single input. Liver perfusion that previously was determined only by transendothelial transport of the contrast agent into the extravascular-extracellular space from a single vascular input function, now contemplates two distinct vascular inputs. It is possible to study with more accuracy and more detail, if there are different contributions from either one of the vascular inputs to the perfusion and quantify them.

From the parametric maps, not only was it possible to point differences in the venous and arterial contributions to the liver perfusion, but also to see that the model was susceptible to detect variations of perfusion after treatment. It was possible establish a classification of treatment responsive (Patients 1 and 3) and non-treatment responsive for patients (Patients 2, 4 and 5), based on, respectively, the decrease and increase of the global liver perfusion after three months of treatment. An interesting result was the ability to detect an increased venous perfusion in one of the responsive patients (Patient 3). As the blood perfusion to the tumor is considered to be mainly arterial, in the case of this patient there is a reestablishment of the blood supply from the portal vein followed by a decrease in the arterial one, stating that treatment was effective in the decrease of the tumor blood perfusion.

Values of K^{trans} from Tofts model were found in the literature for many types of tumors with different sizes, staging and aggressiveness. Taking for example a particular study [32] values of 0,11 and 0,10 s^{-1} were found for K^{trans} respectively in a liver hemangioma and metastases, using a CE MRI study. A more similar case, in patients with HCC [8], values in the range of 0,75 – 0,90 s^{-1} for K^{trans} were found in the tumor ROI. The interpretation of K^{trans} is dependent on the tissue involved and on the underlying physiological circumstances, although it is possible to see that the same orders of magnitude are found in k_{1a} and k_{1p} values for the patients of the present study. An interesting follow-up of this study would be to perfusion results for each patients, obtained using both the Tofts model and the proposed model using a histogram analysis in order to quantify tumors' heterogeneity.

In general, it is possible to say that the application of the dual input single-compartment model to clinical data yielded encouraging results and showed the advantages of using mathematical models that better describe the vasculature of the liver to analyze perfusion data. Nevertheless, this study contains some weaknesses that should be improved in the future:

I - Intra- and inter-subject variability of the acquisition parameters. The latter were not exactly reproduced from subject to subject and within the same patient, also sometimes not exactly reproduced from pre- to post-treatment acquisitions. This led to

different acquisition geometries that made it impossible to use e.g. the same ROIs in pre- and post-treatment analysis. The applied treatment and the disease evolution also induced anatomical changes, particularly to the tumor morphology, also requiring new ROIs definition.

2 - Artifacts due to respiratory motion caused signal dropout that made the identification of structures of interest difficult and invalidated many pixels to be suitable for the application of the model equations because of low SNR.

3 - Limited number of patients used for the software testing. The database, from where data presented in this project was extracted, included more MRI data of patients with hepatocellular carcinoma following the same protocol. However, for many of them, main structures of interest, like portal vein and abdominal aorta, were not included in the imaged slices, making it impossible to apply the dual-input single compartment model to this patients.

Limitations of the study precluded the application of this approach to a larger sample of clinical data. Nevertheless, software implementation has been successfully accomplished and producing treatment sensitive perfusion results.

Chapter 6

Conclusion

Liver hemodynamics is a main determinant of hepatic function. The assessment of liver perfusion remains controversial regarding the variable model-based approaches than can be used.

This work represents a “proof of concept”, i.e. the main objective of this thesis was not to create a perfect algorithm of perfusion parameters calculation, but to demonstrate that it was possible to perform the implementation of a model with assumptions that better describe the liver vascular system, when compared to the traditional Tofts model. A more accurate perfusion assessment through models that better reflect the real vascular architecture of the liver, may help to characterize and predict the onset of malignancies as well as to study the effectiveness of therapies. The implemented software was tested in a particular clinical case of limited data from patients with hepatocellular carcinoma, however patients with other liver perfusion diseases could have been used for the same purpose.

Future work may focus on the clinical validation of the developed software. Strategies involve the development of a complete user interface for the software in order to extend perfusion quantification in the liver to clinical routine. Tests with more patients will allow longitudinal studies and statistical inference. Furthermore, standard operating procedures with specific set of pulse sequence parameters should to be established.

References

- [1] P. S. Tofts and a G. Kermode, "Measurement of the blood-brain barrier permeability and leakage space using dynamic MR imaging. I. Fundamental concepts.," *Magn. Reson. Med.*, vol. 17, no. 2, pp. 357–67, Feb. 1991.
- [2] V. D. Wynsberghe, C. R. Noback, and C. Robert, *Human Anatomy and Physiology*, 3rd edition. New York, NY: McGraw-Hill, Inc, 1995, p. 872.
- [3] S. K. Saladin, *Anatomy and Physiology. The Unity of Form and Function.*, Second Edition. New York: McGraw-Hill Companies Inc., 2001.
- [4] V. Mitra and J. Metcalf, "Functional anatomy and blood supply of the liver," *Anaesth. Intensive Care Med.*, vol. 13, no. 2, pp. 52–53, Feb. 2012.
- [5] C. H. Thng, "Perfusion magnetic resonance imaging of the liver," *World J. Gastroenterol.*, vol. 16, no. 13, p. 1598, 2010.
- [6] F. A. Longo Dan, *Harrison's Gastroenterology and Hepatology*, 18th ed. McGraw Hill Professional, 2010, p. 752.
- [7] P. V Pandharipande, G. A. Krinsky, H. Rusinek, and V. S. Lee, "Perfusion imaging of the liver: current challenges and future goals.," *Radiology*, vol. 234, no. 3, pp. 661–73, Mar. 2005.
- [8] M. a Haider, F. a Farhadi, and L. Milot, "Hepatic perfusion imaging: concepts and application.," *Magn. Reson. Imaging Clin. N. Am.*, vol. 18, no. 3, pp. 465–75, Aug. 2010.
- [9] F. X. Bosch, J. Ribes, M. Díaz, and R. Cléries, "Primary liver cancer: Worldwide incidence and trends," *Gastroenterology*, vol. 127, no. 5, pp. S5–S16, Nov. 2004.
- [10] A. P. Venook, C. Papandreou, J. Furuse, and L. L. de Guevara, "The incidence and epidemiology of hepatocellular carcinoma: a global and regional perspective.," *Oncologist*, vol. 15 Suppl 4, pp. 5–13, Jan. 2010.
- [11] C. L. Tinkle and D. Haas-Kogan, "Hepatocellular carcinoma: natural history, current management, and emerging tools.," *Biologics*, vol. 6, pp. 207–19, Jan. 2012.
- [12] B. R. Greenberger N., Blumberg R., *Current Diagnosis and Treatment: Gastroenterology, Hepatology and Endoscopy*. New York, NY: McGraw-Hill Companies, 2009, p. 580.
- [13] T. Harrison, *Harrison Medicina Interna*, 11^a ed. Rio de Janeiro RJ: Editora Guanabara, 1988, p. volume 2.

- [14] M. J. Sands and A. Levitin, "Basics of magnetic resonance imaging," *Semin. Vasc. Surg.*, vol. 17, no. 2, pp. 66–82, Jun. 2004.
- [15] Haacke Mark, Brown Robert, Thompson Michael, and Venkatesan Ramesh. *Magnetic Resonance Imaging, physical principles and sequence design*. Wiley-Liss, 1999.
- [16] R. M. Van Geuns, P. A. Wielopolski, H. G. De Bruin, B. J. Rensing, P. M. A. Van Ooijen, M. Hulshoff, M. Oudkerk, and P. J. De Feyter, "Resonance Imaging," vol. 42, no. 2, pp. 149–156, 1999.
- [17] C. J. Aine, "A conceptual overview and critique of functional neuroimaging techniques in humans: I. MRI/fMRI and PET.," *Crit. Rev. Neurobiol.*, vol. 9, no. 2–3, pp. 229–309, Jan. 1995.
- [18] D. S. MacDonald-Jankowski, "Magnetic Resonance Imaging. Part I: the Basic Principles," *Asian J. Oral Maxillofac. Surg.*, vol. 18, no. 3, pp. 165–171, Sep. 2006.
- [19] T. Karamitsos and S. Neubauer, "Cardiovascular magnetic resonance imaging," *Medicine (Baltimore)*, vol. 42, no. 8, pp. 461–467, Aug. 2014.
- [20] M. O. Leach, K. M. Brindle, J. L. Evelhoch, J. R. Griffiths, M. R. Horsman, a Jackson, G. C. Jayson, I. R. Judson, M. V Knopp, R. J. Maxwell, D. McIntyre, a R. Padhani, P. Price, R. Rathbone, G. J. Rustin, P. S. Tofts, G. M. Tozer, W. Vennart, J. C. Waterton, S. R. Williams, and P. Workman, "The assessment of antiangiogenic and antivascular therapies in early-stage clinical trials using magnetic resonance imaging: issues and recommendations.," *Br. J. Cancer*, vol. 92, no. 9, pp. 1599–610, May 2005.
- [21] P. S. Tofts, "Modeling tracer kinetics in dynamic Gd-DTPA MR imaging.," *J. Magn. Reson. Imaging*, vol. 7, no. 1, pp. 91–101.
- [22] P. S. Tofts, "Optimal detection of blood-brain barrier defects with Gd-DTPA MRI—the influences of delayed imaging and optimised repetition time.," *Magn. Reson. Imaging*, vol. 14, no. 4, pp. 373–80, Jan. 1996.
- [23] R. Materne, B. E. Van Beers, M. Smith, I. Leconte, J. Jamart, J. P. Dehoux, a Keyeux, and Y. Horsmans, "Non-invasive quantification of liver perfusion with dynamic computed tomography and a dual-input one-compartmental model.," *Clin. Sci. (Lond)*, vol. 99, no. 6, pp. 517–25, Dec. 2000.
- [24] J. M. Llovet, S. Ricci, V. Mazzaferro, P. Hilgard, E. Gane, J.-F. Blanc, A. C. de Oliveira, A. Santoro, J.-L. Raoul, A. Forner, M. Schwartz, C. Porta, S. Zeuzem, L. Bolondi, T. F. Greten, P. R. Galle, J.-F. Seitz, I. Borbath, D. Häussinger, T. Giannaris, M. Shan, M. Moscovici, D. Voliotis, and J. Bruix, "Sorafenib in advanced hepatocellular carcinoma.," *N. Engl. J. Med.*, vol. 359, no. 4, pp. 378–90, Jul. 2008.
- [25] J. Buxeraud, "Gadovist - gadobutrol," *Actual. Pharm.*, vol. 48, no. 490, pp. 47–48, 2009.

- [26] “Image J 1.48 - Image Processing and Analysis in Java.” [Online]. Available: imagej.nih.gov/ij/download/. (accessed on July 2014)
- [27] “RadiAnt DICOM Viewer 1.9.16,” *Medixant*. [Online]. Available: <http://www.radiantviewer.com/>. (accessed on July 2014)
- [28] G. Helms, H. Dathe, N. Weiskopf, and P. Dechent, “Identification of signal bias in the variable flip angle method by linear display of the algebraic Ernst equation.,” *Magn. Reson. Med.*, vol. 66, no. 3, pp. 669–77, Sep. 2011.
- [29] H. Lu, C. Clingman, X. Golay, and P. C. M. van Zijl, “Determining the longitudinal relaxation time (T1) of blood at 3.0 Tesla.,” *Magn. Reson. Med.*, vol. 52, no. 3, pp. 679–82, Sep. 2004.
- [30] R. Materne, A. M. Smith, F. Peeters, J. P. Dehoux, A. Keyeux, Y. Horsmans, and B. E. Van Beers, “Assessment of hepatic perfusion parameters with dynamic MRI.,” *Magn. Reson. Med.*, vol. 47, no. 1, pp. 135–42, Jan. 2002.
- [31] H. P. Gavin, “The Levenberg-Marquardt method for nonlinear least squares curve-fitting problems,” pp. 1–17, 2013. [Online]. Available: <http://people.duke.edu/~hpgavin/ce281/lm.pdf>
- [32] K. Coenegrachts, J. Ghekiere, V. Denolin, B. Gabriele, G. Hérigault, M. Haspelslagh, P. Daled, S. Bipat, J. Stoker, and H. Rigauts, “Perfusion maps of the whole liver based on high temporal and spatial resolution contrast-enhanced MRI (4D THRIVE): feasibility and initial results in focal liver lesions.,” *Eur. J. Radiol.*, vol. 74, no. 3, pp. 529–35, Jun. 2010.

